J Mater Sci (2019) 54:13045–13069

Review

Free-standing transition metal oxide electrode architectures for electrochemical energy storage

Michael A. Spencer[1] and Veronica Augustyn[1,*]

[1] *Department of Materials Science and Engineering, North Carolina State University, Raleigh, NC 27695, USA*

Received: 26 April 2019
Accepted: 2 July 2019
Published online:
12 July 2019

© Springer Science+Business Media, LLC, part of Springer Nature 2019

ABSTRACT

Electrochemical energy storage is becoming more ubiquitous in the world, and with that comes an urgent need for increased performance. One promising approach in the pursuit of next-generation energy storage with simultaneous high energy and high power is through cooperative assembly of electrochemically active materials into conductive scaffolds. In such architectures, the active material is often directly bonded to the conductive scaffold, therefore reducing the need for separate binders and current collectors. The conductive scaffold material can also provide a robust, free-standing structure that is capable of enduring mechanical deformation, which is particularly important for high gravimetric capacity materials that can undergo significant volume changes during electrochemical cycling. This review summarizes several of the most common approaches for developing free-standing binder-free electrode architectures of transition metal oxides that aim to achieve simultaneous high energy and high power for the next generation of electrochemical energy storage devices.

Introduction

Electrochemical energy storage (EES) via batteries and electrochemical capacitors is increasingly ubiquitous in today's digital world. EES devices are powering the portable electronics revolution, from cell phones to tablets and smart watches. The high efficiency of electrical-to-chemical energy conversion coupled with advances in the energy density, power density, and cost of these devices are also increasing their use in the transportation sector and sustainable grids. Continued research and development of EES will shape the future of these applications and their impact in our daily lives. For example, further advances in high-power EES systems will improve the harvesting and storage of intermittent renewable energy sources such as wind and solar. Introducing large-scale EES into the power grid will decrease the demand for fossil fuels and hopefully reduce the environmental impact from existing electricity generation methods [1, 2]. EES could also enable a revolution in electric powered transportation, reducing the amount of global petroleum combustion [3–5]. For EES to reach its potentially tremendous impact on sustainable technology and human well-being, there are further scientific hurdles to overcome, including

Address correspondence to E-mail: vaugust@ncsu.edu

https://doi.org/10.1007/s10853-019-03823-y

achieving simultaneous high power and energy density, decreasing cost, increasing safety, and improving lifetime [6–8].

Most EES devices today store energy in solid-state electrodes [9–11]. Since the electrochemical redox reaction occurs on the solid material's interface with the electrolyte, and because (in the case of batteries) the reacted species must also undergo solid-state diffusion into the bulk of the particle, there are several fundamental requirements for the electrodes. First, since electrochemical reactions require both electron and ion motion to and from the electrochemical interface, the electrodes must be both electronically and ionically conductive. This requirement can be difficult to satisfy simultaneously in many materials, and as a result, the electrodes contain micro- or nanoscale particles to decrease diffusion distances and increase porosity as well as conductive additives to increase electronic conductivity. Another basic requirement for solid-state EES electrodes is that they must store high amounts of energy by volume and area. To do this, it is important to utilize high gravimetric capacity active materials, but the final volumetric and areal energy densities are determined by the electrode architecture. Ideally, the electrodes are thick (hundreds of microns or more in thickness) as well as dense to provide high areal and volumetric energy densities. This is also difficult to satisfy simultaneously, and most electrodes are either thin and dense or thick and highly porous.

To meet these requirements, traditional solid-state EES electrodes are fabricated via the casting of a slurry that consists of micron to hundred nanometer-sized particles of the electrochemically active material, a high surface area conductive additive, and a polymer binder [12]. Due to the number of components, there are many factors that affect the final electrode architecture, including the active material size, conductive additive size, and binder concentration, to name a few. This approach has been optimized for micron-size, roughly spherical particles often utilized in lithium-ion batteries. However, scientists still lack a thorough understanding of how each processing parameter or condition individually affects the final electrode architecture [13], which leads to difficulties when applying this methodology to non-spherical and/or nanosized particles. Due to the many variables involved in slurry casting, there is always the possibility that the electrode architecture is not consistent from batch to batch, which can result in poor energy storage performance. Furthermore, the electrode architecture fabricated from slurries does not simultaneously promote high energy density and high power density because of sub-optimal electron and ion transport pathways. To illustrate this point, scanning electrochemical cell microscopy of single particles of $LiMn_2O_4$ showed facile de/intercalation of Li^+ at rates as high as 1 V s^{-1}—but when the particles were assembled into slurry electrodes, these rapid kinetics disappeared due to poor ion and electron transport in the electrode architecture [14]. It is hypothesized that electrode architectures that provide more control over the transport of ions and electrons—so-called deterministic architectures—would be better for providing both high power and high energy densities [15].

Recently, the United States Department of Energy Office of Basic Energy Sciences reported the need for "tunable functionality of materials and chemistries that enable holistic design for energy storage" as well as the need to achieve simultaneous high energy and high power [16]. Since design of electrodes and their energy and power performance are intimately related, these will require detailed understanding of the kinetics and mechanisms of electrochemical reactions occurring at solid-state electrode interfaces, as well as predictive control over the electrode architecture.

One promising approach in the pursuit of next-generation energy storage with simultaneous high energy and high power is through cooperative assembly of electrochemically active materials into conductive scaffolds [15, 17, 18]. Figure 1 conceptualizes the hierarchical structures that can be defined by the conductive scaffold or the ordered assembly of conductive materials. It is important to note that in such architectures, the active material is often directly bonded to the conductive material, therefore reducing the need for separate binders and current collectors. Advances in synthesis techniques, such as hydrothermal synthesis [19], electrodeposition [20], and atomic layer deposition [21, 22], have enabled conformal deposition of nanostructured active materials onto a variety of conductive scaffolds. The conductive scaffold material can also provide a robust, free-standing structure that is capable of enduring mechanical deformation, which is particularly important for high gravimetric capacity materials that can undergo significant volume changes during electrochemical cycling. If the conductive scaffold has a high surface area, this could enable high active

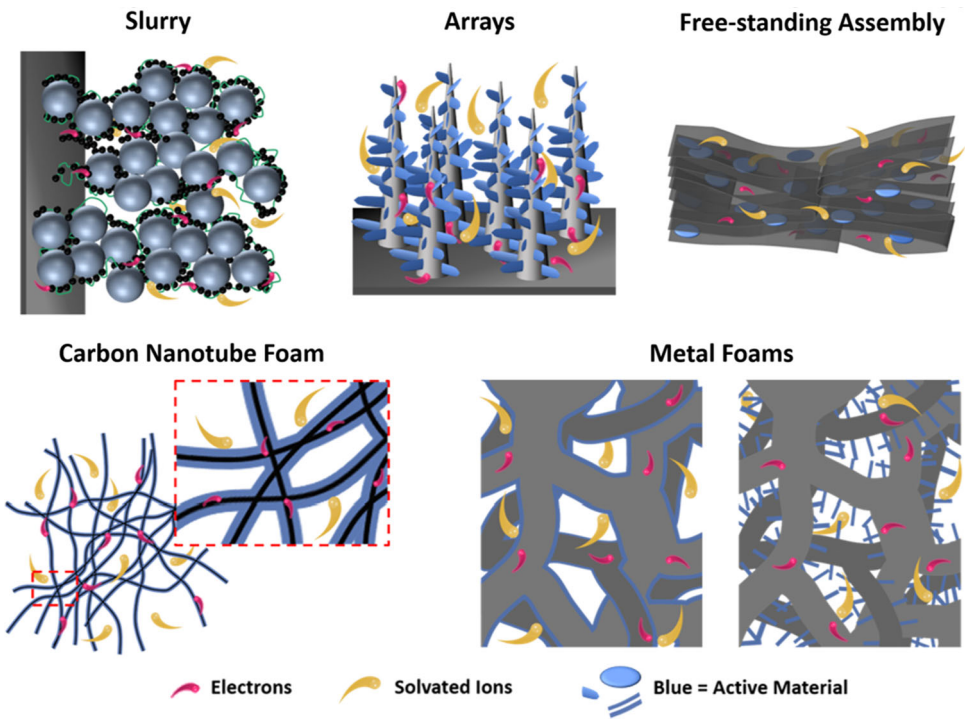

Figure 1 The morphology of the commercially utilized slurry electrode for EES can result in insufficient electron and ion transport to the active material. Emerging deterministic electrode architectures, such as arrays, assemblies, and metal and carbon foams, provide well-defined electron transport paths and porosity for improved utilization of the active material, as shown schematically in the figure.

material loading and therefore high areal capacity. Achieving high areal capacity is necessary to match the areal capacity of high energy density anodes such as Li metal and silicon [23]. This review summarizes several of the most common approaches for developing free-standing binder-free electrode architectures of transition metal oxides (TMO) that aim to achieve simultaneous high energy and high power for the next generation of electrochemical energy storage. Several other reports have summarized the importance of electrode architecture on EES [17, 24–28].

Transition metal oxides for electrochemical energy storage

TMOs have several advantages as active materials for EES. In general, they can deliver a high theoretical capacity due to the number of accessible valence states of transition metal ions, which is directly related to the number of electrons that can be stored per formula unit. Compared to transition metal sulfides, TMOs have higher ionicity which leads to higher redox potentials [29]. High redox potentials are needed for cathodes in high energy density batteries. TMOs can undergo faradaic EES via several different mechanisms: (1) pseudocapacitance, whereby the redox occurs at the surface or is not limited by solid-state diffusion [30]; (2) intercalation of ions into the bulk while the host structure retains its overall morphology [31]; and (3) decomposition and conversion, whereby the oxide undergoes reversible reduction into a suboxide or the transition metal itself [32]. The general trend is that the capacity, and energy density, is highest for TMOs undergoing conversion or decomposition and lowest for those undergoing only pseudocapacitive charge storage. The power density, energy efficiency, and lifetime tend to trend in the opposite way, with the fastest, most efficient, and durable storage obtained with pseudocapacitive materials. It should be noted that the conversion reaction mechanism is plagued by inherent voltage hysteresis even at slow rates, which results in low energy efficiency [32].

TMOs can undergo EES reactions with a variety of cations, including protons [33], Li^+ [34], Na^+ [35], and K^+ [36], in aqueous, non-aqueous, ionic liquid, and solid-state electrolytes. Furthermore, TMOs exhibit a variety of crystalline structures, such as layered, olivine, or spinel phases, that enable fast ion diffusion pathways [30]. These structures can be tuned to improve the EES properties, by, for example, inducing oxygen vacancies [37] or introducing species such as water molecules in the interlayer [38]. The TMO surfaces can also be modified to prevent undesirable reactions with the electrolyte by

depositing a more stable TMO or carbon coating [39, 40]. TMOs can be synthesized via several scalable approaches without the need for special atmospheres, making them attractive for industrial applications [19]. There are also several methods for depositing nanostructured TMOs onto a conductive scaffold, such as chemical bath deposition [41–44], hydrothermal reaction [36, 45], atomic layer deposition [46–48], and electrodeposition [35, 49, 50]. In many cases, such synthesis results in good adhesion between the TMO and the scaffold, which can lead to low charge transfer resistance and long cycling stability—negating the need for electrochemically inactive conductive additives and binders. Furthermore, these nanostructured TMO deposits benefit from improved tolerance to pulverization during charging/discharging [51, 52].

Metrics to evaluate performance

Evaluating and comparing the performance of advanced energy storage electrode architectures can only be possible when sufficient metrics are provided to do the analysis. However, this can be complicated as the reported metrics vary depending on the mechanism of energy storage (for example, pseudocapacitance vs. conversion reactions) and the intended application. In general, however, it is best practice to report the electrode mass loading (both active material and total mass including binder, conductive additive and/or scaffold), the footprint area, and the overall thickness. This way, gravimetric, areal, and volumetric capacities and energy densities can be readily calculated for electrodes even if they are not directly discussed in the manuscript. Moreover, future data mining of the energy storage literature (in order to comprehensively benchmark new electrode architectures) would significantly benefit from the proper reporting of these parameters.

Hierarchical arrays and assemblies for free-standing electrode architectures

Free-standing TMO-based electrode architectures have been developed through (1) the formation of nanoarrays on flat substrates and (2) assembly of materials into a hierarchical structure.

Arrays on a flat substrate

The general concept for this electrode architecture is to grow or deposit micron or nanoscale ordered arrays onto a flat substrate, thereby increasing the total surface area and decreasing diffusion distances as well as the contact resistance due to the improved adhesion of the active material to the current collector. However, the areal mass loading that can be reached without sacrificing EES performance is limited to less than 1 mg cm^{-2}, which is directly related to the limited thickness of the array (typically less than 10 microns). This is due to the low electronic conductivity of most TMOs in their fully oxidized state [53]. Nanoarrays of TMOs can be obtained by multiple approaches. One is to directly synthesize TMO nanostructures on the surface of a conductive substrate [54–57]. Wu et al. [45] used a two-step hydrothermal synthesis to first grow Co_3O_4 nanowire arrays on Ti foil, and subsequently grow Fe_2O_3 branches, as shown in Fig. 2a. Electrochemical analysis of the conversion reactions of Co_3O_4 and Fe_2O_3 with Li^+ was carried out in a non-aqueous electrolyte. The high-frequency electrochemical impedance spectroscopy revealed a lower charge transfer resistance for the 5-μm-thick Co_3O_4@Fe_2O_3 array electrode as compared to electrodes with only Co_3O_4 or Fe_2O_3 arrays on the Ti substrate. Using a similar approach, Xia et al. [42] hydrothermally grew Co_3O_4 nanowire cores on a conductive glass substrate followed by chemical bath deposition of NiO shells. The Co_3O_4/NiO arrays, with a thickness of ~ 10 μm, were electrochemically characterized in an alkaline aqueous electrolyte. It was hypothesized that the rate capability and cycling stability of the Co_3O_4/NiO electrode arrays were improved as compared to only the Co_3O_4 or the NiO arrays due to sufficient electronic conductivity of the Co_3O_4 nanowires and additional capacity and structural support provided by the NiO shells. Nanostructured TMOs deposited on a flat substrate can obtain good rate capability and cycling stability. However, the limited thickness of the electrochemically active material limits the achievable areal capacity.

Metal and carbon supports can also be grown from the surface of flat substrates to produce reliable electronic conduction pathways to/from the current collector [58, 59]. For example, Xu et al. [49] grew a Ni nanowire array via a magnetic-field-driven selective deposition growth process on Ti foil, which was then

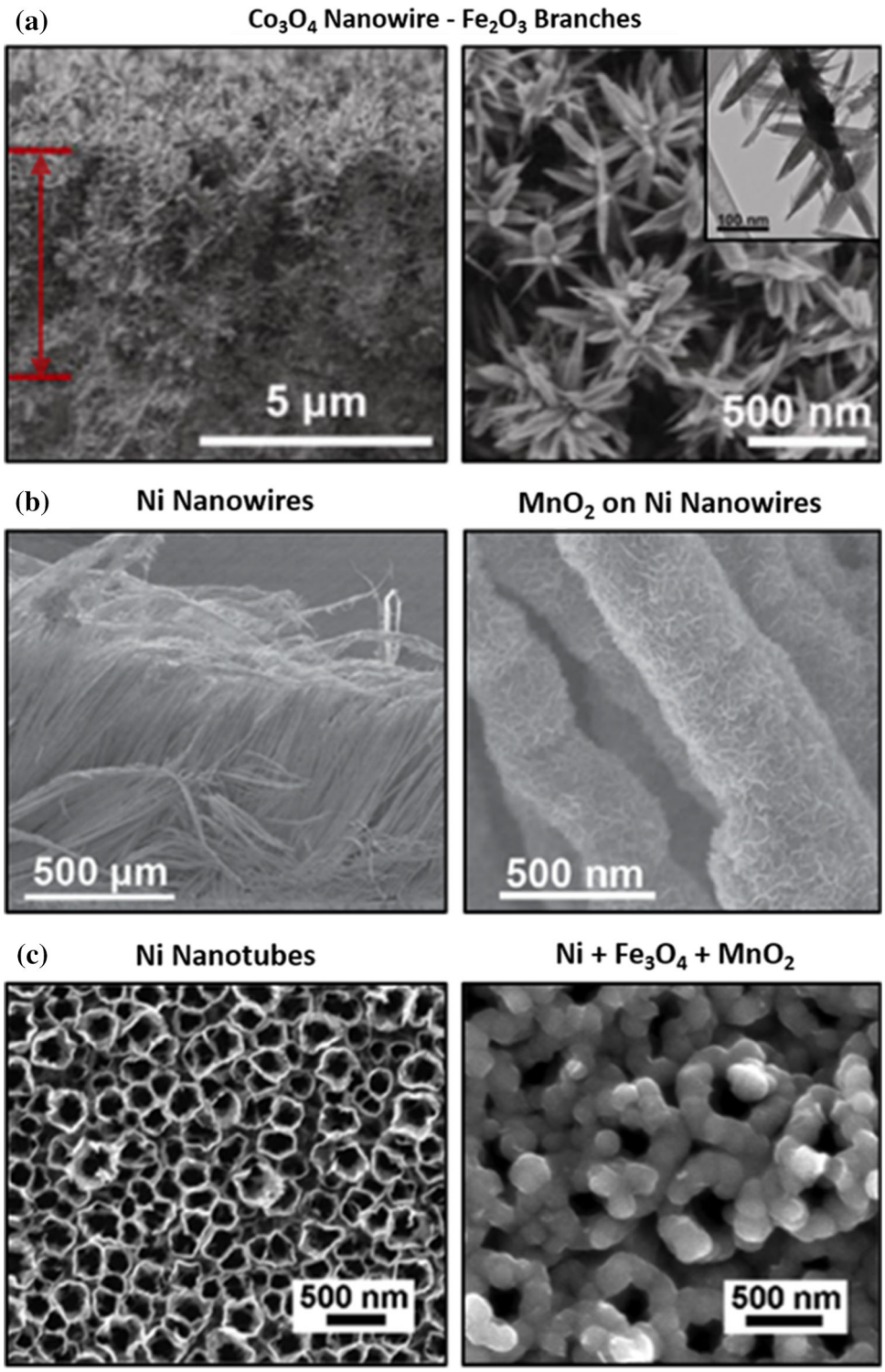

Figure 2 **a** Scanning electron micrographs of the cross-section (left) and top-down view (right) and transmission electron micrograph (inset) of Fe_2O_3 branches grown on Co_3O_4 nanowires (adapted with permission from Ref. [45], Copyright 2013 Springer Nature), **b** low-magnification cross-section (left) and a high-magnification (right) scanning electron micrographs of nickel nanowires with MnO_2 electrodeposited on the surface (adapted with permission from Ref. [49]. Copyright 2016 John Wiley and Sons), and **c** scanning electron micrographs of nickel nanotubes (left) and nickel nanotubes electrodeposited with Fe_3O_4 and MnO_2 which are uniformly distributed throughout the array electrode (adapted with permission from Ref. [50]. Copyright 2017 John Wiley and Sons).

used as a scaffold for the electrodeposition of MnO_2, as shown in Fig. 2b. The length of the Ni nanowires was approximately 1 mm, which provided electron transport paths through thicker electrodes compared to the electrodes that were only composed of TMOs. To determine the pseudocapacitive behavior of this electrode, cyclic voltammetry was performed in a Na_2SO_4 aqueous electrolyte between 0 and 0.8 V versus a saturated calomel electrode (SCE). It was found that the areal capacitance increased as active

material loading increased, and an electrode with an active material loading of 17 mg cm^{-2} had an areal capacitance of ~ 2.5 F cm^{-2} at 1 mV s^{-1}. Furthermore, a Ni nanoarray electrode with 3.5 mg cm^{-2} MnO_2 retained its initial capacitance after 20,000 cycles at 10 mA cm^{-2}, indicating that electrodeposition onto the Ni nanowire array provided sufficiently strong adhesion to survive many charge/discharge cycles.

Another type of architecture synthesized on a flat conducting substrate is the bicontinuous inverse opal structure [60–62]. Liu et al. [63] synthesized an inverse opal V_2O_5/graphene composite electrode and investigated its EES performance as a Li^+ intercalation cathode in a non-aqueous electrolyte. Polystyrene spheres deposited on tungsten foil were used as templating agents for the inverse opal architecture, followed by the deposition of Ni, graphene, and V_2O_5. Subsequent etching of the polystyrene and Ni left behind only a V_2O_5/graphene composite electrode on tungsten. Even after 2000 cycles at a rate of 5 C, a 6-μm-thick electrode retained a capacity of 203 mAh g^{-1} (based on the mass of the full electrode). A commercial Ni foam sacrificial scaffold was also used to synthesize a 100-μm-thick electrode. The capacity of the thick electrode after 1000 cycles at a 5 C rate was 198 mAh g^{-1}. This study demonstrated that the bicontinuous electron transport and electrolyte diffusion pathways enabled high capacity and cycle life in the V_2O_5/graphene inverse opal architecture.

Another strategy to develop a hierarchical electrode architecture is to synthesize porous metal foils. Hou et al. [64] fabricated porous copper by chemically dealloying magnetron-sputtered copper manganese. Subsequently, MnO_2 was plated on the nanoporous Cu using an electroless plating technique. Since the MnO_2 was directly plated on the Cu surface, there was good electron transport throughout the electrode layer and the porous structure was maintained for electrolyte diffusion. The electrochemical characterization was performed by cycling in a Li^+ non-aqueous electrolyte between 0.01 and 3.0 V versus Li/Li^+ to determine the performance of the electrode for the full conversion reaction of MnO_2 to metallic Mn. This architecture accommodated the significant volume changes during the repeated conversion between MnO_2 and metallic Mn, and the capacity retention was more than 90% after 1000 cycles at 8.4 A g^{-1}. Tubular metals have also been shown as effective electrode scaffolds for oxides undergoing conversion reactions [65]. Figure 2c shows Ni nanotubes grown by Li et al. [50] using an electrochemical alloying/dealloying process. Using two subsequent electrodeposition processes, Fe_3O_4 nanoparticles were grown on the Ni nanotube arrays followed by a shell of MnO_2, which added to the overall capacity and was hypothesized to protect the Fe_3O_4 nanoparticles from pulverization brought on by the conversion reaction during electrochemical cycling in a $LiPF_6$ electrolyte. This electrode architecture had a capacity retention of 42.6% upon increasing the rate from 0.2 to 8 C. Furthermore, between the 2nd and 1000th cycle, the capacity retention was ~ 96% when cycling at a 1 C rate. Overall, synthesizing nanostructured conductive materials on a flat substrate enables the electronic conductivity necessary for thick energy storage electrodes.

Assemblies

Electronically conductive nanostructured materials can be assembled in such a way that they form hierarchical structures with good electronic and ionic conductivity. Carbon materials such as carbon nanotubes (CNTs) [46, 66] and graphene [67] are prime candidates for this type of approach. Recently, Xu et al. [68, 69] reported a holey graphene conductive assembly with tunable porosity suitable for fast electrolyte and ion diffusion. Sun et al. [70] combined solutions of graphene oxide and Nb_2O_5 precursor, which formed a free-standing electrode after two freeze-drying and annealing steps (Fig. 3). This structure allowed for an oxide mass loading of up to 22 mg cm^{-2}. The Li^+ intercalation behavior of the Nb_2O_5/holey graphene framework electrode was compared to a Nb_2O_5/graphene framework electrode (graphene without nanopores) by cycling in a $LiPF_6$ non-aqueous electrolyte. As the charge/discharge rate increased from 1 to 100 C, the Nb_2O_5/holey graphene framework electrode showed superior performance compared to the Nb_2O_5/graphene framework, as demonstrated in Fig. 3. When both were tested with a Nb_2O_5 loading of 6 mg cm^{-2} at a 100 C rate, the Nb_2O_5/holey graphene framework had a capacity of 75 mAh g^{-1}, while the Nb_2O_5/-graphene framework had a capacity of only 35 mAh g^{-1}. The effect of mass loading on the gravimetric capacity was also investigated, and it was

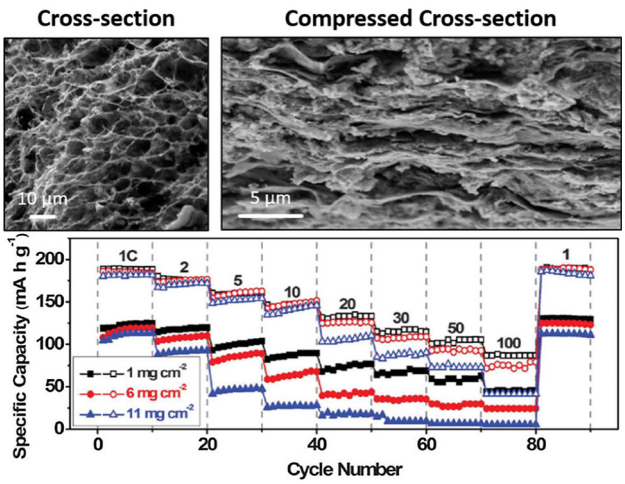

Figure 3 (top) Cross-sectional scanning electron micrographs of the Nb_2O_5/holey graphene framework before and after compression. (Bottom) The specific capacity measured during galvanostatic charge/discharge tests in a $LiPF_6$ non-aqueous electrolyte shows that the Nb_2O_5/holey graphene electrodes (hollow) exhibit higher capacity than the Nb_2O_5/graphene electrodes (filled) at rates between 1 and 100 C and for three different Nb_2O_5 loadings. Adapted with permission from Ref. [70]. Copyright 2017 American Association for the Advancement of Science.

found that the Nb_2O_5/holey graphene framework had better capacity retention than the Nb_2O_5/-graphene framework and Nb_2O_5/graphene (with no framework structure). These results demonstrated that holey graphene is a promising scaffold for TMOs particularly at the high mass loadings necessary for many applications.

Free-standing metal oxide nano- and microstructures grown on porous substrates

Foams and sponges

Many metal foams are commercially available, while other, more advanced carbon foams can now be synthesized. These structures are in many ways ideal supports for TMOs. The hierarchical structure of a metal foam exhibits high surface area for active material support, macropores for easy electrolyte diffusion, and interconnected electronically conductive pathways. These attributes enable high active material loading per footprint area, which is a key requirement for high areal capacity. Electrically conductive foam scaffolds are compatible with several synthesis approaches, including in situ growth [71, 72], electrodeposition [42] and, most commonly, hydrothermal synthesis [36, 73–76]. These approaches enable control of morphology, size, and mass of the deposited material, allowing for good tunability of the final electrochemical behavior. The nanostructure of the TMO in contact with the foam architecture leads to good electrolyte accessibility to the electrochemically active sites and reduces the ion diffusion path lengths within the TMO.

Metal foams

Nickel foam and copper foam scaffolds are particularly interesting because they can be purchased at low cost and require very little preparation prior to TMO synthesis. The mechanically robust, macroporous architecture of the Ni foams provides open channels for electrolyte absorption and transport, as well as reliable metallic conduction throughout electrodes with initial thicknesses that can reach several millimeters. When using these foams as scaffolds for EES, it is important to keep in mind the redox activity of the foam itself, along with any native surface oxides that are present. A prominent example of this is the redox activity of Ni foam in alkaline electrolytes. Several studies demonstrated simple synthesis techniques that effectively incorporate nanostructured TMO arrays on the surfaces of Ni foam [36, 73, 74, 77–80] and copper foam [81–83]. For example, Wu et al. [36] used hydrothermal synthesis to grow MnO_2 on the surface of Ni foam. As shown in Fig. 4a, the resulting electrode architecture consisted of MnO_2 nanosheets extending from the surface of micron-sized plate-like MnO_2 directly adhered to the Ni foam scaffold. The adhesion between MnO_2 and the Ni foam scaffold was beneficial for efficient electron transport, while the hierarchical structure enabled good oxide mass loading, high MnO_2/electrolyte interfacial area, and short ion diffusion distances.

The electrochemical performance and stability of TMOs on Ni foam can be further improved by the addition of a layer or array of carbon, such as graphene nanosheets or CNTs, between the nickel and the TMO [75, 84, 85]. The Ni foam architectures with a carbon array proved to be more effective than bare Ni foam for accommodating the strain induced by large volume expansions of the active material during charging/discharging [71]. Zhai et al. [86]

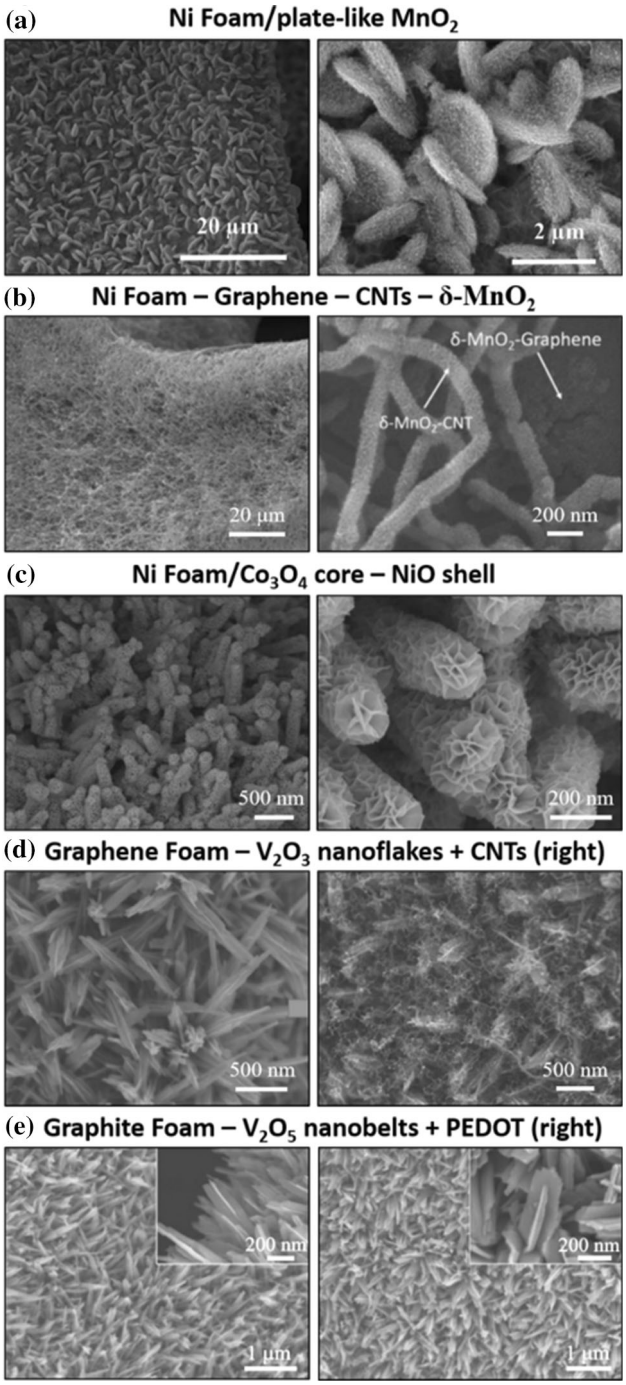

◀**Figure 4** Scanning electron micrographs of TMOs grown on foam scaffolds: **a** MnO_2 nanosheet-on-plates grown on a Ni foam scaffold (adapted with permission from Ref. [36]. Copyright 2018 Elsevier); **b** graphene and CNTs were initially grown on a Ni foam scaffold, followed by hydrothermal growth of δ-MnO_2 on the carbon surfaces (adapted with permission from Ref. [86]. Copyright 2018 Elsevier); **c** core–shell Co_3O_4 nanowire-NiO nanosheet grown on a Ni foam scaffold (adapted with permission from Ref. [42]. Copyright 2012 American Chemical Society); **d** V_2O_3 grown on graphene foam via solvothermal synthesis (left) and V_2O_3 with CNTs grown on the surface via chemical vapor deposition (right) (adapted with permission from Ref. [88]. Copyright 2016 John Wiley and Sons); **e** V_2O_5 nanobelts grown on graphite foam (left) with subsequently electropolymerized PEDOT, which uniformly coated the V_2O_5 surface (adapted with permission from Ref. [89]. Copyright 2014 John Wiley and Sons).

demonstrated the growth of both graphene flakes and CNTs from Ni foam, followed by the growth of δ-MnO_2 (birnessite) via a hydrothermal reaction, as shown in Fig. 4b. The graphene and CNTs provided additional electronic transport paths and increased the scaffold surface area, which enabled the filling of more pore volume with the δ-MnO_2 active material. The conversion reaction of the electrode was tested in a $LiPF_6$ electrolyte. The high-frequency region of the Nyquist plot obtained via electrochemical impedance spectroscopy showed a reduction in the size of the semicircle. This was attributed to a reduction in the charge transfer resistance during the conversion reaction of MnO_2 to metallic Mn. In a related approach, Jia et al. [87] hydrothermally synthesized metal oxide nanosheets containing manganese and cobalt onto Ni foam. Subsequent annealing of the electrode in air led to the formation of MnO_2 nanosheets which had pores filled with cobalt nanospheres. These cobalt nanospheres subsequently served as catalysts and growth sites for the plasma-enhanced chemical vapor deposition of CNTs. These CNTs grew through pores in the MnO_2 nanosheets and entangled between the nanosheets to form an interconnected conductive network. The capacitive energy storage performance of the CNT/MnO_2 composite on Ni foam was tested in a Na_2SO_4 aqueous electrolyte. The CNT/MnO_2 on Ni foam electrode showed better cycling stability as compared to Co-MnO_2 on Ni foam, retaining $\sim$ 95% and 63% of the initial capacity, respectively, after 10,000 cycles at 10 A g^{-1}. Carbon nanostructures integrated with metal foams or nanostructured TMOs can lead to a higher surface area to support TMO deposits and more pathways for electronic conduction.

Another approach to improve the electrochemical performance of TMOs deposited on metal foams is by growing core–shell structures of two different TMO materials [76, 90, 91]. Xia et al. [42] demonstrated this idea through the synthesis of Co_3O_4 nanowire/NiO nanoflake core–shell arrays grown on Ni foam,

shown in Fig. 4c. Electrochemical characterization was carried out in an aqueous KOH electrolyte. Upon increasing the rate from 2 to 40 A g^{-1}, the capacitance retentions for the Ni foam + Co_3O_4/NiO, Ni foam + Co_3O_4, and Ni foam + NiO were 85%, 76.7%, and 66.6%, respectively. For the same electrodes, the capacitance retentions after cycling for 6000 cycles at 2 A g^{-1} were 95.1%, 85.5%, and 56.7%, respectively. These capacitance retentions were based on the maximum capacity that was reached after some activation period during the first ~ 1000 cycles. Two advantages of using the Co_3O_4/NiO core/shell architecture were (1) the Co_3O_4 was sufficiently electronically conductive (extending the electron transport paths to more NiO) and (2) the NiO shell improved the mechanical stability during the continuous electrochemical activation process throughout the first ~ 1000 cycles.

Carbon-based foams

In addition to providing better electrochemical stability, carbon-based foams generally provide higher surface area and lower mass density, particularly as compared to metal foams. The lower mass density is important to achieve high gravimetric energy and power densities. In comparison with metal foams, which can be 10–15 mg cm^{-2}, carbon-based foams have achievable mass densities of < 1 mg cm^{-2} [89]. These free-standing, electrically conductive carbon-based materials are also suitable for the TMO synthesis protocols used for metal foams.

The carbon foam substrates that are most commonly used are graphene foam [92] and CNT foam [66, 93, 94]. Similar to what was discussed for metal foams, it is possible to grow CNTs from the surface of the graphene foam, which increase the surface area for TMO growth while still providing suitable electron transport pathways. Guan et al. [95] deposited nanocrystalline Fe_2O_3 on CNT forests on graphene foam. These electrode architectures demonstrated good cycling stability in an aqueous KOH electrolyte. After 50,000 cycles at 20 mA cm^{-2}, the average capacity retention was 97%. While 50,000 cycles exceed the EES cycle life requirements for portable electronics, this result demonstrates the ability of the architecture to extend EES device lifetime, which is critical for transportation and grid storage applications. Additionally, Xia et al. [88] demonstrated that growing TMO nanostructures on graphene foam and subsequently growing CNT forests on the TMO surface is another viable approach to improve charge transport throughout thick electrodes. Figure 4d shows the graphene foam + V_2O_3/CNT and the graphene foam + V_2O_3 electrode architectures that were compared in this study. Galvanostatic charge/discharge experiments in a $NaPF_6$ non-aqueous electrolyte were used to characterize the intercalation of Na^+ into V_2O_3. The impact of the electrode architecture was evident at fast charge/discharge rates. Upon increasing the current density from 2 to 10 A g^{-1}, the capacity retention of the composite with CNTs was 52%, whereas that of the composite without CNTs was only ~ 6%.

Instead of growing CNTs on the TMOs, Chao et al. [89] used solvothermal synthesis to grow V_2O_5 on graphene foam and then electrodeposited poly(3,4-ethylenedioxythiophene) (PEDOT) on the V_2O_5 surface. Control of the electropolymerization of EDOT (3,4-ethylenedioxythiophene) led to the formation of a thin layer of PEDOT on the V_2O_5 and graphene foam, as shown in Fig. 4e. This composite exhibited a good cycling stability in a $LiPF_6$ non-aqueous electrolyte for the intercalation of Li^+ into V_2O_5, with 98% capacity retention after 1000 cycles at 60 C. It was hypothesized that the PEDOT layer was able to accommodate the volume expansion of the V_2O_5 and potentially reduced the polarization at the electrode at high C-rates. The results highlight the utility of conductive polymer coatings on TMOs for additional electronic conductivity as well as strain accommodation. Another benefit is that most can be deposited at low temperatures, decreasing cost and avoiding thermally induced structure and morphological changes.

Chen et al. [72] modified a CNT sponge with hydrothermally grown Co_3O_4 nanoparticles by a densification and compaction procedure, which was a simple approach to achieve high areal capacity. To achieve higher mass density, the CNT sponge was compressed by a factor of about 10 to allow the electrode to fit into a coin cell. The increase in density is evidenced in the scanning electron micrographs in Fig. 5a, b. The Co_3O_4 mass was kept at approximately 60% of the total electrode mass. As the thickness of the CNT sponge was increased from 2 to 5 mm, the amount of Co_3O_4 mass per area increased from 7.3 to 14.3 mg cm^{-2}. Thus, the thickness of the CNT sponge was used to tune the active material loading. The sponge electrode was subsequently compacted to a

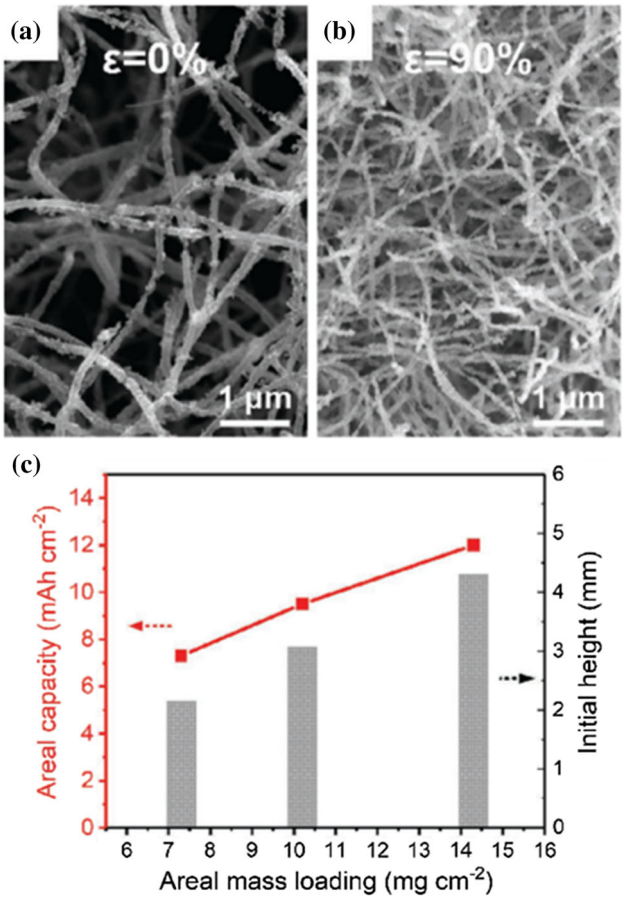

Figure 5 Scanning electron micrographs of Co_3O_4/CNT sponges from 0% strain **a** to 90% strain **b** show the effect of strain on densification; **c** areal capacity increases with increased Co_3O_4 mass loading, which is controlled by the initial height of the CNT sponge. Adapted with permission from Ref. [72]. Copyright 2018 John Wiley and Sons.

thickness between 0.2 and 0.4 mm. The compacted electrode architecture with 50% strain was tested in a $LiPF_6$ non-aqueous electrolyte for the conversion from Co_3O_4 to metallic Co between 0.01 and 3.0 V versus Li/Li^+. As shown in Fig. 5c, this final electrode architecture led to an increase in areal capacity with mass of Co_3O_4, which allowed the electrode to reach the active material loading necessary for many commercial applications (> 10 mg cm^{-2}). Upon increasing the active material loading, impedance spectroscopy revealed a small increase in charge transfer resistance while the areal capacity increased nearly linearly. Based on these results, it was concluded that the densification led to a trade-off between increased electrical conductivity and reduced porosity (which possibly restricted electrolyte diffusion). Ultimately, this approach provides a path toward controlling the electrode architecture via a top-down method to obtain high areal capacity.

Textiles

Textiles, such as carbon cloths, felts, and papers, can also serve as free-standing substrates for TMO electrodes. They are typically composed of micron-sized carbon fibers. These fibers are mechanically quite stable and as a result offer reliable electron transport pathways. Compared to foams, textiles typically exhibit lower surface area, but they offer the advantages of low-cost and scalable processing.

Carbon cloths and felts

Carbon cloths and felts are commonly used as flexible, conductive scaffolds that offer higher surface area compared to foils. They allow for continuous electron transport paths and eliminate inactive materials such as conductive additives and binders. Carbon cloths and felts are particularly beneficial for electrodes for flexible energy storage devices [35, 44, 96–99], which could be used in smart textiles. Carbon fibers can also be used to design devices in a rope or twisted configuration [100]. Furthermore, carbon cloths and felts are compatible with several TMO syntheses, such as chemical bath deposition [41, 43, 44], atomic layer deposition [47, 48], hydrothermal synthesis [47, 48, 96, 101–104] and electrodeposition [35, 97, 100].

Liu et al. [41] used chemical bath deposition to grow $ZnCo_2O_4$ nanoplate arrays on carbon cloth. The oxide nanoplate-on-carbon cloth architecture, shown in Fig. 6a, had several advantages, such as good electron conduction paths through carbon fibers, short ion diffusion lengths in the nanoplates, and adhesion between the oxide and carbon substrate. This led to good cycling stability during the conversion reaction between $ZnCo_2O_4$ and lithium in a non-aqueous Li^+ electrolyte. The conversion reaction involved both Zn and Co and led to a capacity of ~ 3 mAh cm^{-2} after 100 cycles at 0.24 mA cm^{-2}. Using electrodeposition, Huang et al. [35] synthesized MnO_2 nanosheets on carbon cloth. At a synthesis temperature of 60 °C, ε-MnO_2 nanosheets formed on the carbon cloth followed by the growth of hollandite (α-MnO_2) nanorods on the surface of the

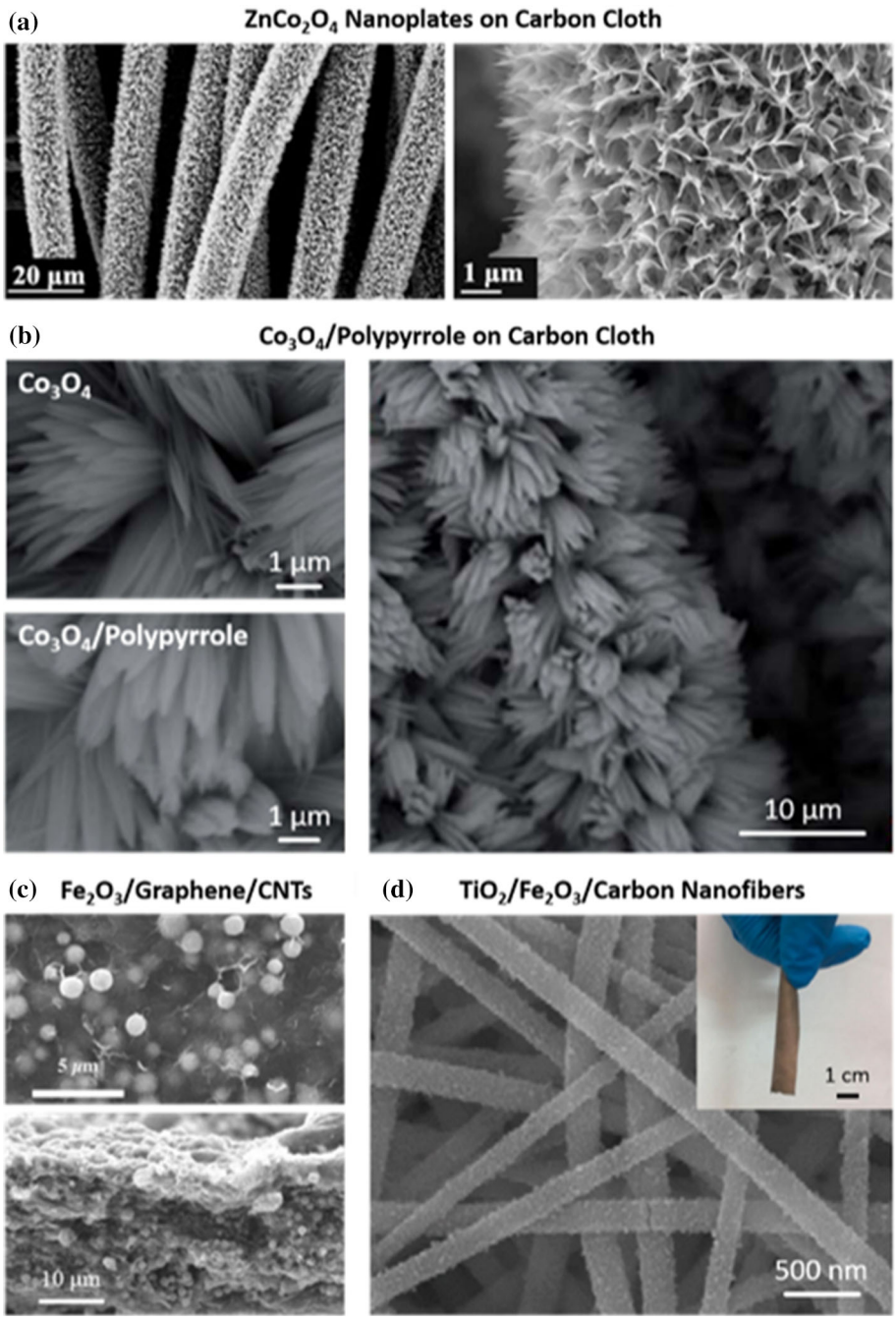

Figure 6 Scanning electron micrographs of nanostructured TMOs on carbon textile architectures and in carbon paper electrode architectures: **a** $ZnCo_2O_4$ nanoplates uniformly grown on carbon fibers in a carbon cloth electrode via chemical bath deposition (adapted with permission from Ref. [41]. Copyright 2018 Elsevier); **b** Co_3O_4 nanorod bundles hydrothermally grown on a carbon cloth architecture that was uniformly coated with polypyrrole via electropolymerization (adapted with permission from Ref. [98]. Copyright 2018 Royal Society of Chemistry); **c** Fe_2O_3 distributed throughout a binder-free graphene/CNT composite paper electrode architecture (adapted with permission from Ref. [83]. Copyright 2015 Elsevier); **d** electrospun composite TiO_2/carbon nanofibers with Fe_2O_3 nanoparticles grown on the surface via a vapor–solid reaction (adapted with permission from Ref. [34]. Copyright 2019 Elsevier).

nanosheets. The cycling stability and lack of morphology change of the electrode after cycling suggested that the MnO_2 nanosheet/nanorod on carbon cloth architecture accommodated the strain due to Na^+ de/intercalation during cycling in an aqueous 1 M Na_2SO_4 electrolyte. An electrode with an active material mass loading of 10 mg cm^{-2} showed an overall increase in capacity after 2000 cycles, which was ascribed to some type of activation process during the first 200 cycles. It was hypothesized that the interface between the α-MnO_2 nanorods and ε-MnO_2 nanosheets, along with the increase in active material-electrolyte interfacial area, led to better electrochemical performance as compared to a carbon cloth electrode that contained only the nanosheets.

Huang et al. [97] electropolymerized poly(vinylpyrrolidone) on carbon cloth and subsequently annealed the electrode and electrodeposited V_2O_5, resulting in a V_2O_5/carbon nanowire array on carbon cloth. This electrode architecture led to good

rate capability during Li^+ intercalation to/from V_2O_5 in an aqueous LiCl electrolyte, retaining 52.4% of the capacity when the current increased from 1 to 100 mA cm^{-2}. This electrode architecture was used in a 2 V flexible asymmetric supercapacitor device, which retained 91% of the capacitance after 8000 cycles at a rate of 40 mA cm^{-2}.

Conductive polymers have been incorporated into TMO/carbon cloth composite electrodes, similar to approaches taken using foam architectures. Ma et al. [98] used a hydrothermal reaction to grow Co_3O_4 nanorod bundles on carbon cloth followed by the electropolymerization of polypyrrole in a core–shell architecture, as shown in Fig. 6b. Electrochemical analysis was carried out in an aqueous KOH electrolyte. This architecture proved to be advantageous based on the higher capacity of the Co_3O_4@-polypyrrole electrode compared to just Co_3O_4 nanorod bundles, presumably due to the polypyrrole layer facilitating electron transfer. The Co_3O_4@-polypyrrole electrode had a capacity retention of 97.4% upon increasing the current density from 2 to 20 mA cm^{-2}, and the capacity was stable after 2000 cycles.

Zheng et al. ball-milled $LiCoO_2$ and incorporated it into carbon cloth along with a smaller scale conductive additive (Ketjenblack). The resulting electrode exhibited a high areal capacity of 28 mAh cm^{-2} for Li^+ de/intercalation in a non-aqueous electrolyte [23]. It was hypothesized that in high active material loading electrodes, conductive pathways must be present at multiple length scales to effectively distribute charge [105]. Using this approach, an electrode with a $LiCoO_2$ loading of 213 mg cm^{-2} reached a discharge capacity of $\sim$ 28 mAh cm^{-2} at 0.8 mA cm^{-2}. For an electrode with a $LiCoO_2$ loading of 71 mg cm^{-2}, the capacity retention was $\sim$ 70% upon increasing the rate from 0.8 to 1.6 mA cm^{-2}. The integration of conductive materials with different dimensions thus enables high active material loading and therefore areal capacity. Further research will be necessary to understand how the various conductive additives interact with the TMOs to provide sufficient electronic transport even at high rates.

Electrode papers

Free-standing electrode paper architectures can also be utilized as scaffolds for TMOs. The fabrication of the papers can be as simple as vacuum filtration [106] or via more complicated techniques such as floating catalyst chemical vapor deposition [107]. Electrode papers can also be made via a scalable electrospinning technique that has become a popular synthesis approach to obtain interconnected electron transport throughout thick electrodes [108]. Wang et al. [83] utilized the vacuum filtration procedure to synthesize a composite electrode of Fe_2O_3, CNTs and graphene oxide shown in Fig. 6c. The surface area of this composite was 37.8 m^2 g^{-1}, indicating that this route does not lead to very high surface area electrodes. The EES performance of these electrode papers was investigated for the conversion reaction of Fe_2O_3 in a non-aqueous Li^+ electrolyte. After 120 cycles at 50 mA g^{-1}, the electrode had a high reversible capacity of 716 mAh g^{-1}, which was higher than either a graphene-CNT composite or Fe_2O_3 electrode. The performance improvements of the composite electrode were attributed to better electron transport and electrolyte diffusion throughout the electrode architecture. It was also hypothesized that the graphene and CNTs support the Fe_2O_3 nanoparticles and prevent cracking during cycling, which is particularly beneficial in conversion reactions which lead to large volume changes.

More complex techniques for fabricating electrode papers, such as electrospinning, lead to better control over the nanostructure and porosity than vacuum filtration [108–110]. Yang et al. electrospun TiO_2 nanofibers in polyvinyl pyrrolidone and calcined them in a nitrogen atmosphere to carbonize the polymer. The resulting TiO_2/carbon nanofibers were then soaked in iron chloride hexahydrate and heated in an autoclave in the presence of ammonia to obtain the nanostructured Fe_2O_3/TiO_2/carbon nanofibers shown in Fig. 6d [34]. The fibrous electrode architecture allowed for a high electrode–electrolyte interfacial area in a Li^+ non-aqueous electrolyte as well as sufficient electronic transport throughout the electrode. This supported the Li^+-driven conversion reaction of Fe_2O_3 and intercalation reaction of Li^+ into TiO_2. Kong et al. [111] also used the electrospinning technique to form V_2O_5 nanosheets that were subsequently encapsulated in carbon using chemical vapor deposition. Electrochemical analysis in a Li^+ non-aqueous electrolyte showed that the capacity was close to the theoretical value for the intercalation of 2 Li^+ per V_2O_5, and the capacity retention was 91.7% after 200 cycles at a 0.5 C rate. Furthermore, the electrode architecture had good

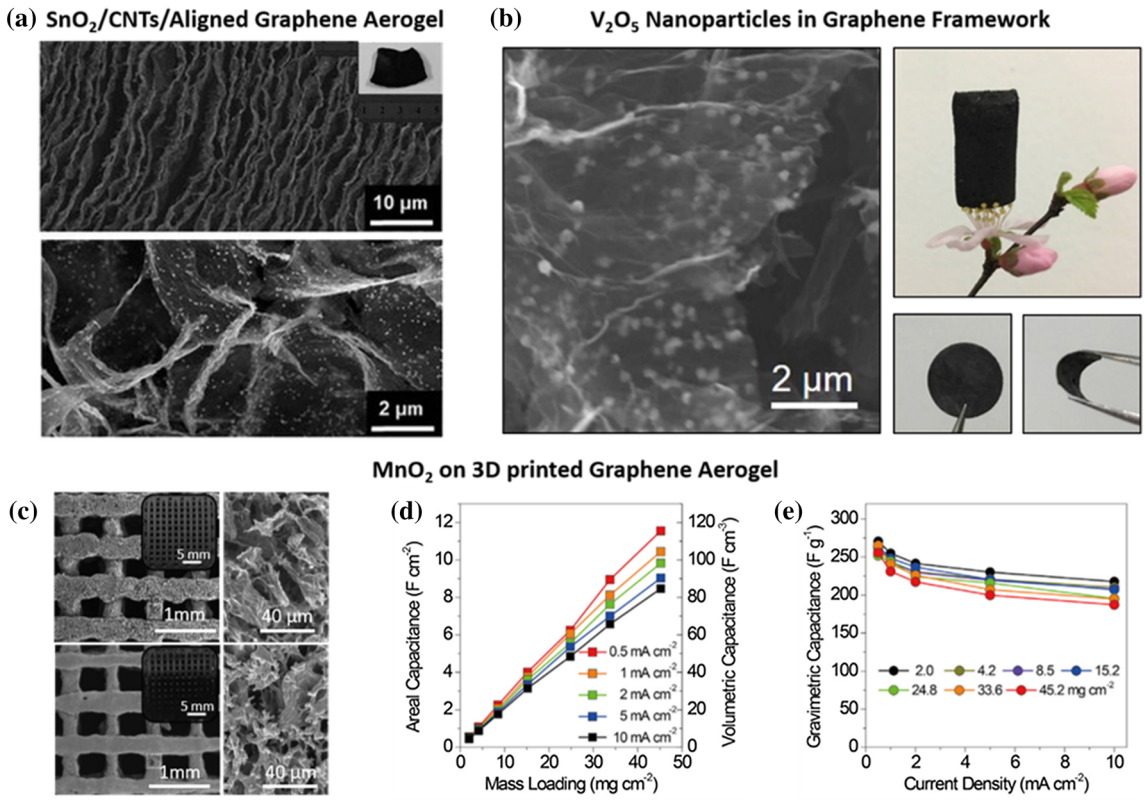

Figure 7 **a** Scanning electron micrographs of SnO_2 nanoparticles and CNTs dispersed in a vertically-aligned graphene aerogel, and an optical image of the free-standing electrode (inset) (adapted from Ref. [120]. Licensed under CC BY 4.0); **b** Scanning electron micrographs and optical images of a flexible, free-standing graphene framework electrode architecture with V_2O_5 nanoparticles uniformly dispersed on the carbon surface (adapted with permission from Ref. [121]. Copyright 2018 Elsevier); **c** Scanning electron micrographs and optical micrographs (insets) of a 3D-printed graphene aerogel with electrodeposited MnO_2 and **d** corresponding electrochemical analysis that demonstrate that the areal capacitance of the electrode increased linearly with increased MnO_2 areal loading and **e** the relatively consistent decrease in gravimetric capacitance as charge/discharge rate increased for electrodes with MnO_2 loading between 2 and 45.2 mg cm^{-2} (adapted with permission from Ref. [122]. Copyright 2019 Elsevier).

electronic transport and electrolyte diffusion pathways, which was demonstrated by the retention of 40% of the capacity when cycling from 0.1 to 100 C (36 s discharge or charge). Electrospun fiber papers have emerged as an interesting architecture for free-standing electrodes that exhibits flexibility, good stress accommodation, and sufficient electronic and electrolyte diffusion paths through a simple and scalable synthesis procedure.

Aerogels

Aerogels present a promising high surface area architecture that enables good electron transport and porosity for both active material deposition and electrolyte diffusion [18, 112]. Some aerogels are even reversibly compressible, making them viable candidates for flexible next-generation batteries [113]. Although there have been many examples of aerogel electrodes that use binders [114, 115], there are some successes in binder-free aerogels [116–119]. For example, Liu et al. [120] formed aerogels of vertically aligned graphene sheets separated by CNTs and octahedral SnO_2 nanocrystals, as shown in Fig. 7a. This architecture led to good contact between the conductive carbon materials and the active SnO_2, while ensuring good permeability of the Li^+ non-aqueous electrolyte throughout the channels of the aerogel. The good contact was particularly important for the conversion reaction of SnO_2. In addition to good rate capability, the aerogel electrode was capable of retaining 80% of the initial capacity after cycling 1000 times at a 0.1 C rate. Furthermore, Gao et al. [121] used a N-doped graphene aerogel

framework to deposit V_2O_5 nanoparticles via a hydrothermal method. Figure 7b shows how the resulting aerogels contained nanoparticles that were well adhered to, and encapsulated by, the graphene sheets. These composite aerogels accommodated the volume expansion of the V_2O_5 during intercalation of Li^+ from a non-aqueous electrolyte, with a capacity of 283 mAh g^{-1} and a capacity retention of ~ 78% after 500 cycles at 1 A g^{-1}. Furthermore, the capacity retention was 71% upon increasing the current density from 100 to 1000 mA g^{-1}. These studies indicate that aerogels could provide the electronic conductivity and ion transport needed for high-energy and high-power electrodes; however, further research is needed to develop binder-free electrodes with higher active material loading.

Yao et al. [122] reported the fabrication of a 3D printed graphene electrode architecture using a direct ink writing method that was subsequently used as the substrate/working electrode for the electrodeposition of nanostructured MnO_2, as shown in Fig. 7c. The active material mass loading was controlled by the electrodeposition time. This electrode architecture demonstrated good electrochemical intercalation of Li^+ in an aqueous LiCl electrolyte. Figure 7d, e shows that areal capacitance increased linearly from ~ 0.5 to 11.55 F cm^{-2} at 0.5 mA cm^{-2} when mass loading increased from 2 to 45.2 mg cm^{-2}, while the gravimetric capacitance remained relatively constant. This proved that most of the active material was utilized for energy storage even at the higher mass loading. The scalability of this method was demonstrated with a 4-mm-thick electrode that had an MnO_2 mass loading of 182.2 mg cm^{-2}. This electrode achieved a high areal capacitance of 44.13 F cm^{-2} at a rate of 0.5 mA cm^{-2}. This example highlights the potential for 3D printing to be integrated into the manufacturing of free-standing TMO electrodes. Additional research will be necessary to push the resolution limits of the 3D printing process, which currently leads to large porosity which decreases the volumetric energy density.

Electrode architectures for solid-state battery cathodes

Solid-state batteries with inorganic solid electrolytes are increasingly being considered for next-generation EES with improved energy density and safety than existing Li-ion batteries. Inorganic solid-state batteries have the potential to replace flammable organic liquid electrolytes due to recent improvements in ionic conductivity of inorganic solid electrolytes [123]. Furthermore, when such electrolytes are paired with Li metal and other Li alloys they could lead to higher energy densities than existing EES [124]. Many research efforts have focused on developing solid electrolytes with high ionic conductivity and investigating the interface stability between the electrolyte and electrodes [125–131]. Several promising electrolyte materials have been tested, including various sulfides, oxysalts, and oxides, perhaps most notably cubic garnet type oxides such as lithium lanthanum zirconate (LLZO) [132, 133]. Although there are several challenges that must be addressed with ISEs, especially at the electrode/electrolyte interfaces [134], it is critical to also develop new electrode architectures for cathodes with high active material loading in contact with solid electrolytes [135, 136]. Of particular importance for these new electrode architectures is to develop and maintain a high electrochemical interface area between the solid electrolyte and electrode during electrochemical cycling.

Thus far, most reports on inorganic electrolyte-based solid-state batteries use a cathode that was prepared via slurry processing. Unlike the slurry electrodes fabricated for liquid electrolyte-based EES, these consist of the cathode active material, conductive additive, and inorganic solid electrolyte powder in order to ensure high interfacial area between the cathode and electrolyte [137]. However, there are emerging attempts to develop more advanced architectures for better contact between the active material and current collector (for electronic transport) and active material and solid electrolyte (for ionic transport) [136]. The importance of increasing the interfacial contact between the electrolyte and composite electrode was recently illustrated by van den Broek et al. [138]. The electrochemical behavior of a solid-state battery with an "interface-engineered" LLZO was compared to a flat electrolyte pellet, as shown in Fig. 8a. Both cells contained cathodes fabricated from slurries of $Li_4Ti_5O_{12}$ active material, LLZO electrolyte powder, polyvinylidene fluoride (PVDF), and conductive carbon particles. Through electrochemical impedance spectroscopy and equivalent circuit modeling, it was evident that the resistance of the interface-engineered full cells was reduced by more

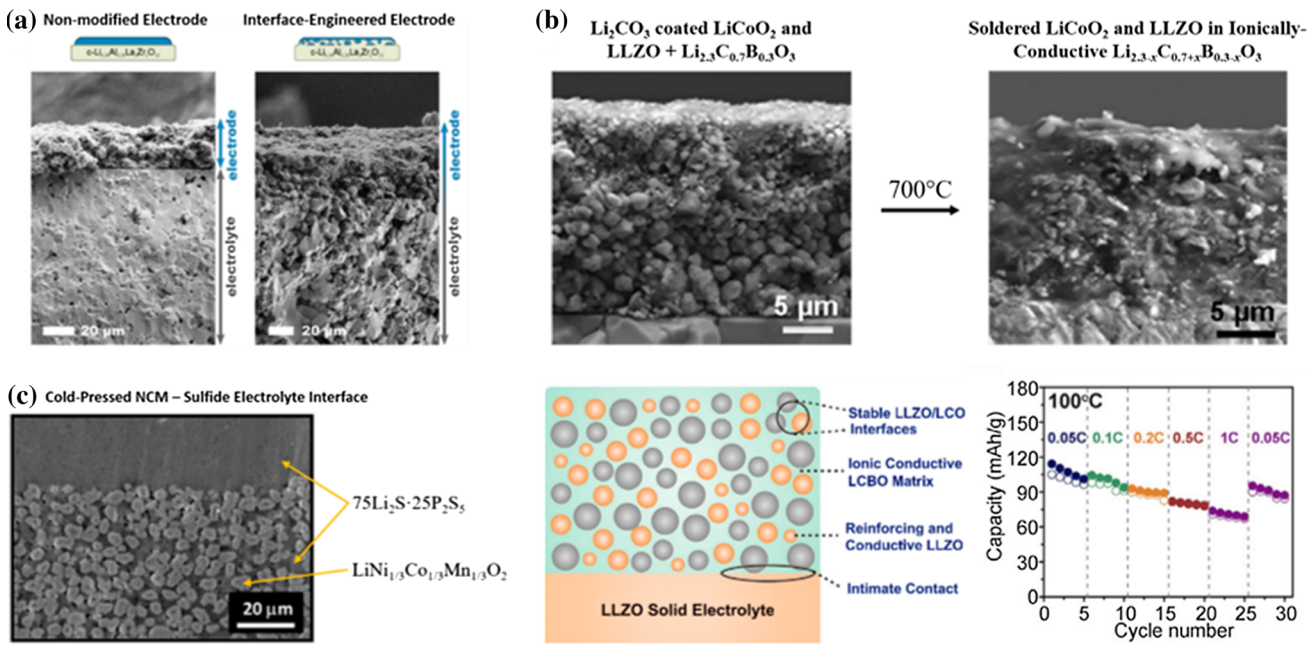

Figure 8 Electrode architectures found in solid-state batteries with inorganic solid electrolytes: **a** Scanning electron micrographs that demonstrate the improved integration of solid-state battery slurry electrodes into a porous interface-engineered LLZO electrolyte as compared to the slurry deposited on an unmodified LLZO pellet (adapted with permission from Ref. [138]. Copyright 2016 John Wiley and Sons); **b** scanning electron micrographs before and after soldering of $LiCoO_2$ particles to LLZO particles using a matrix of $Li_{2.3}C_{0.7}B_{0.3}O_3$, a schematic diagram of the interface and electrochemical analysis showing the capacity retention of an electrode cycled at 100 C at rates ranging from 0.05 to 1 C (adapted with permission from Ref. [139]. Copyright 2018 Elsevier); **c** scanning electron micrograph of the interface formed between a sulfide electrolyte and NCM active particles after compression of the composite pellet (adapted with permission from Ref. [140]. Copyright 2016 Elsevier).

than a factor of two. Furthermore, the gravimetric capacity obtained from galvanostatic charge/discharge experiments showed up to a tenfold increase in capacity for the interface-engineered electrodes, which was largely attributed to a decrease in the charge transfer resistance at the active material-electrolyte interface. Wang et al. [139] developed a thermal soldering technique to engineer the interface between $LiCoO_2$ and LLZO. LLZO particles and $LiCoO_2$ particles were coated with Li_2CO_3 and $Li_{2.3}C_{0.7}B_{0.3}O_3$, mixed together, and deposited onto a Li_2CO_3-coated LLZO pellet. The composite electrode and electrolyte were then sintered at 700 °C, which caused the $Li_{2.3}C_{0.7}B_{0.3}O_3$ to react with the Li_2CO_3 and form ionically conductive $Li_{2.3-x}C_{0.7+x}B_{0.3-x}O_3$ (LCBO). The resulting electrode architecture, shown in Fig. 8b, prevented interdiffusion between the $LiCoO_2$ and LLZO due to their separation by the LCBO matrix. Surprisingly, no additional conductive additives were necessary because apparently the $LiCoO_2$ had sufficient electronic conductivity (even in its delithiated state). The electrochemical performance was first investigated at 100 °C with a $LiCoO_2$ loading of ~ 1 mg cm^{-2} and a Li metal anode. The reversible capacity was ~ 106 mAh g^{-1} at a 0.05 C rate, which was close to the theoretical capacity of 115 mAh g^{-1} for $LiCoO_2$ cycled between 3.0 and 4.05 V versus Li/Li^+. These electrodes retained $\sim 66\%$ of the initial capacity upon increasing the rate from 0.05 to 1 C, as shown in Fig. 8b. Furthermore, the reversible capacity measured at 25 °C was ~ 83 mAh g^{-1} at a 0.05 C rate. There was still some mechanical degradation that occurred due to stresses/strains brought on by $LiCoO_2$ expansion and contraction, which resulted in capacity fade. This last point highlights the need to understand the electro-chemo-mechanics of solid electrolyte–cathode interfaces and to use this knowledge to design better electrode architectures.

Sulfide-based solid electrolytes are attractive because they not only have high ionic conductivity but are mechanically more ductile than oxides, which can mitigate the capacity fading due to mechanical degradation in solid-state batteries [141].

Furthermore, these mechanical properties enable lower temperature processing, such as cold pressing, as compared to solid oxide electrolytes [142]. To prevent the formation of a resistive layer between oxide cathodes and sulfide-based solid electrolytes, several coating layers, including ZrO_2 [143], $LiAlO_2$ [144], $Li_4Ti_5O_{12}$ [145], and $LiNbO_3$ [146], have been investigated. Sakuda et al. [140] demonstrated this approach by spray-coating ~ 10 nm of $LiNbO_3$ onto $LiNi_{1/3}Co_{1/3}Mn_{1/3}O_2$ (NCM). Electrodes consisting of 75 wt% NCM and 25 wt% sulfide electrolyte were pressed to the sulfide electrolyte by applying a pressure of 330 MPa at room temperature. Figure 8c shows that upon decreasing the size of the solid electrolyte particles, there was improved contact and fewer cracks between the NCM and electrolyte. At a low current density and at 30 °C, the size of the NCM and solid electrolyte particles did not affect the capacity, and all of the electrodes delivered a reversible capacity between 140 and 150 mAh g^{-1} at a $C/20$ rate. At increased current densities, electrodes with smaller initial particle sizes for NCM and sulfide electrolyte (5 μm and 4 μm, respectively) delivered the highest reversible capacity with 126 mAh g^{-1} at a $C/2$ rate.

Another strategy to increase the cathode/solid electrolyte interfacial area is to deposit thin films of solid electrolytes on top of three-dimensional cathode

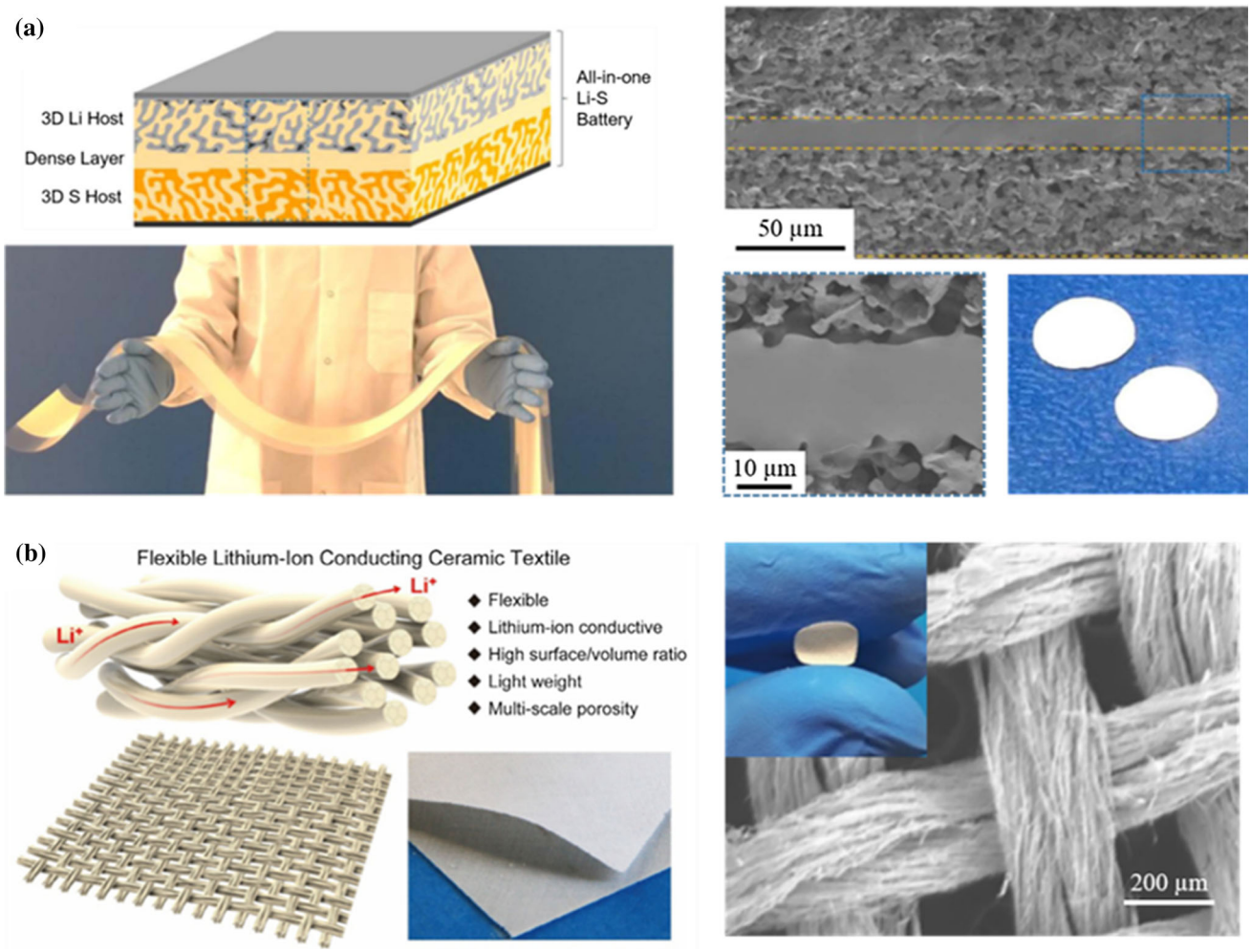

Figure 9 **a** Schematic illustration and scanning electron micrographs of a trilayer porous-dense-porous tape-casted LLZO electrolyte with high surface area for sufficient contact between the electrode materials (in this case Li metal and sulfur) and the electrolyte, and a photograph of a large sheet of the electrolyte demonstrating the scalability of this approach (adapted with permission from Ref. [148]. Copyright 2018 Elsevier); **b** schematic and scanning electron micrograph that illustrate an LLZO ceramic textile that was used to define the electrode architecture, which was demonstrated for a lithium-sulfur battery (adapted with permission from Ref. [149]. Copyright 2018 Elsevier).

arrays. Sun et al. used magnetron sputtering to deposit MoO_3 cathodes. Depending on the deposition temperature, the MoO_3 formed either a 3D vertically oriented nanosheet morphology or a 2D planar morphology. Amorphous lithium phosphate oxynitride (LIPON) was then deposited on top of the MoO_3 nanosheets followed by a ~ 2-μm-thick Li metal anode [147]. Cyclic voltammetry showed that the 3D vertically oriented electrode architecture led to a decrease in cell resistance and polarization and improved Li^+ kinetics as compared to the 2D planar morphology. Furthermore, galvanostatic charge/discharge revealed that the capacity retention of the 3D thin film battery was 41% upon increasing the rate from 50 to 1000 mA g^{-1}, whereas the 2D thin film battery only achieved a capacity retention of 23%. There was also a substantial improvement in the cycling performance of the 3D thin film battery as compared to the 2D thin film battery. Furthermore, the 3D thin film battery had a capacity retention of 92.7%, compared to 76% for the 2D thin film battery, after 1000 cycles at 500 mA g^{-1}. The improvements in rate capability and cycling stability of the 3D thin film battery were attributed to the increased electrode/electrolyte interface area and short Li^+ diffusion lengths.

Another approach is for the solid electrolyte to define the electrode architecture [136]. Vapor deposition techniques, such as ALD and CVD, enable conformal coating of the active material on surfaces with rough or high aspect ratio features such as solid electrolytes [21]. For example, Xu et al. [148] developed a porous-dense-porous trilayer LLZO electrolyte for lithium/sulfur batteries, shown in Fig. 9a, using a scalable tape-casting technique. The thickness of the porous electrode layers was about 50–70 μm, and the thickness of the dense layer separating the two electrodes was 10–30 μm. The anode porous layer was first coated with zinc oxide, which improved the wetting of the subsequently deposited lithium. The cathode porous layer was coated with CNT ink until the surface was visibly dark prior to the infiltration of molten sulfur with a mass loading of 5.4 mg cm^{-2}. The pores within the sulfur electrode were intentionally left slightly unfilled to accommodate the volume expansion during discharge. This electrode architecture achieved a capacity of ~ 1200 mAh g^{-1} at 50 mA g^{-1} (per gram of sulfur) and maintained ~ 90% of the initial capacity after 50 cycles. Gong et al. [149] developed the LLZO textile architecture shown in Fig. 9b using a template method that involved soaking of the textile template in a ceramic precursor followed by pyrolysis to remove the organic components. This architecture was used for a lithium-sulfur battery but was also proposed for TMO cathodes. These emerging strategies will likely pave the way toward the integration of solid electrolytes into commercial applications.

Conclusions and outlook/perspectives

Recent advancements in the synthesis of nanostructured metals, carbons, and TMOs, along with their characterization, have enabled the development of a large number of "beyond slurry" electrode

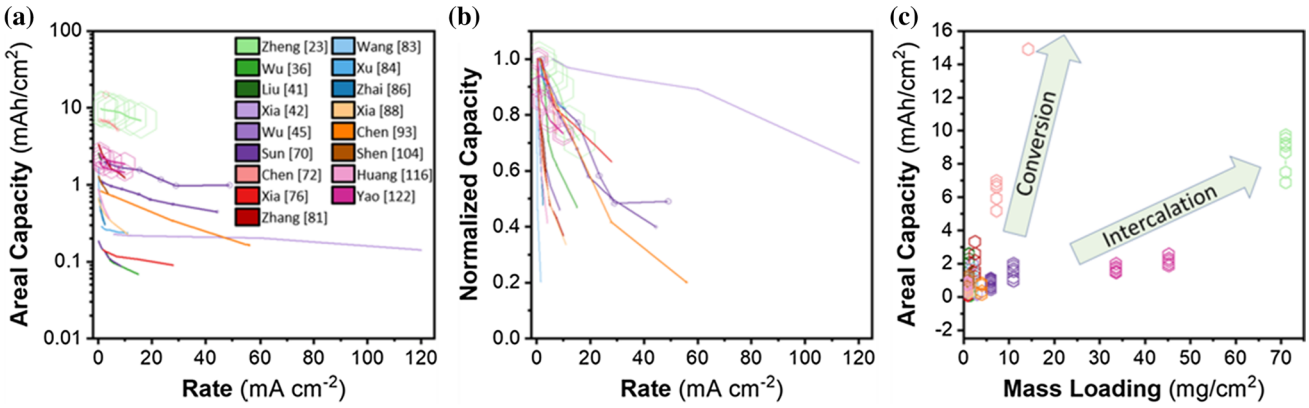

Figure 10 **a** Areal capacity and **b** normalized capacity as a function of applied current and **c** areal capacity as a function of areal mass loading for some of the advanced electrode architectures described here. The size of the data point in **a** and **b** indicates the relative mass loading. While there is great variability in the areal capacity, the rate capability tends to follow similar trends indicating similar kinetic limitations.

architectures for EES. As summarized here, these types of electrode architectures exhibit significantly improved energy storage kinetics as compared to their traditional slurry electrode counterparts and will be necessary for future EES that combines both high power and high energy density. Figure 10 graphically summarizes several of the electrode architectures discussed in this review. First, it should be noted that it is difficult to make this type of comparison because most manuscripts do not provide sufficient detail of all the electrode parameters. Future data mining of electrode architectures would be beneficial to compare new architectures to existing ones, but this will only be possible if sufficient data are reported about the area and volumetric material loading. Figure 10a plots the areal capacity as a function of applied current, and there is great variability in the initial capacity due to different energy storage mechanisms. Figure 10b shows that when the initial capacity is normalized, most of the reported electrode architectures exhibit very similar rate capability indicating similar kinetic limitations. Figure 10c shows that when the areal capacity is plotted as a function of areal mass loading, there is a difference between conversion electrodes and intercalation electrodes. The former do not require high areal mass loading to achieve high areal capacities due to very high gravimetric capacities. Such electrode architectures need to focus more on accommodating the significant volume changes of conversion electrode materials. On the other hand, intercalation-type electrodes do need high areal mass loading and here the focus should be on how to integrate more mass per area.

There are still several open challenges and opportunities for these types of advanced electrodes. First, slurry electrodes benefit from high reproducibility and ease of large-scale manufacturing; "beyond slurry" electrode architectures need to do the same. This has been a challenge for nanostructured materials particularly for small-batch processes. It is likely that electrode architectures that minimize the number of steps required for manufacturing will be most successful. The high cost of nanostructured materials is also an issue. Some techno-economic studies suggest that the manufacturing costs of EES electrodes with carbon felts and CNTs could be similar to current methods; however, these estimates assume decreased costs from increased production (economy of scale) and expected performance improvements such as longer battery life [3, 150, 151]. With the capacity of roll-to-roll slurry manufacturing of Li^+ batteries rapidly expanding, the performance and/or cost of next-generation electrodes needs to far exceed the status quo or be a "drop-in" replacement to existing manufacturing processes. Second, the obtained electrode architectures are still far from deterministic. In this respect, computational finite element modeling should be beneficial to maximize the utilization of the electrode porosity to provide just enough volume for mass loading and electrolyte infiltration. Third, much of the advancement in these next-generation electrode architectures arises from innovation in nanostructured current collectors which need to also be highly scalable and simple to manufacture. Fourth, such architectures are leading the way for the integration of EES with flexible electronics and smart clothing and this is likely to continue. Lastly, these next-generation electrode architectures may enable multi-functionality of EES that is yet to be fully explored, by incorporating, for example, self-healing and self-diagnostic features.

Acknowledgements

Funding was provided by the Research Corporation for Science Advancement (Scialog: Advanced Energy Storage) and Lyda Hill Foundation.

References

[1] Dunn B, Kamath H, Tarascon J-M (2011) Electrical energy storage for the grid: a battery of choices. Science 334:928–935. https://doi.org/10.1126/science.1212741

[2] U.S. Energy Information Administration (2018) Electricity in the United States. https://www.eia.gov/energyexplained/index.php?page=electricity_in_the_united_states. Accessed 2 Mar 2019

[3] Schmuch R, Wagner R, Hörpel G, Placke T, Winter M (2018) Performance and cost of materials for lithium-based rechargeable automotive batteries. Nat Energy 3:267–278. https://doi.org/10.1038/s41560-018-0107-2

[4] Cano ZP, Banham D, Ye S, Hintennach A, Lu J, Fowler M, Chen Z (2018) Batteries and fuel cells for emerging electric vehicle markets. Nat Energy 3:279–289. https://doi.org/10.1038/s41560-018-0108-1

[5] Cox B, Mutel CL, Bauer C, Mendoza Beltran A, van Vuuren DP (2018) Uncertain environmental footprint of current and future battery electric vehicles. Environ Sci Technol 52:4989–4995. https://doi.org/10.1021/acs.est.8b00261

[6] Goodenough JB, Kim Y (2010) Challenges for rechargeable Li batteries. Chem Mater 22:587–603. https://doi.org/10.1021/cm901452z

[7] Etacheri V, Marom R, Elazari R, Salitra G, Aurbach D (2011) Challenges in the development of advanced Li-ion batteries: a review. Energy Environ Sci 4:3243. https://doi.org/10.1039/c1ee01598b

[8] Turcheniuk K, Bondarev D, Singhal V, Yushin G (2018) Ten years left to redesign lithium-ion batteries. Nature 559:467–470. https://doi.org/10.1038/d41586-018-05752-3

[9] Simon P, Gogotsi Y (2008) Materials for electrochemical capacitors. Nat Mater 7:845–854. https://doi.org/10.1038/nmat2297

[10] Cheng F, Liang J, Tao Z, Chen J (2011) Functional materials for rechargeable batteries. Adv Mater 23:1695–1715. https://doi.org/10.1002/adma.201003587

[11] Whittingham MS (2004) Lithium batteries and cathode materials. Chem Rev 104:4271–4302. https://doi.org/10.1021/cr020731c

[12] Liu J, Xu C, Chen Z, Ni S, Shen ZX (2018) Progress in aqueous rechargeable batteries. Green Energy Environ 3:20–41. https://doi.org/10.1016/j.gee.2017.10.001

[13] Kraytsberg A, Ein-Eli Y (2016) Conveying advanced Li-ion battery materials into practice the impact of electrode slurry preparation skills. Adv Energy Mater 6:1600655. https://doi.org/10.1002/aenm.201600655

[14] Tao B, Yule LC, Daviddi E, Bentley CL, Unwin PR (2019) Correlative electrochemical microscopy of Li-ion (De)intercalation at a series of individual $LiMn_2O_4$ particles. Angew Chemie Int Ed 58:4606–4611. https://doi.org/10.1002/anie.201814505

[15] Braun PV, Cook JB (2018) Deterministic design of chemistry and mesostructure in Li-ion battery electrodes. ACS Nano 12:3060–3064. https://doi.org/10.1021/acsnano.8b01885

[16] Department of energy (2017) Basic research needs for next generation electrical energy storage. https://science.osti.gov/bes/Community-Resources/Reports

[17] Long JW, Dunn B, Rolison DR, White HS (2004) Three-dimensional battery architectures. Chem Rev 104:4463–4492. https://doi.org/10.1021/cr020740l

[18] Long JW, Rolison DR (2007) Architectural design, interior decoration, and three-dimensional plumbing en route to multifunctional nanoarchitectures. Acc Chem Res 40:854–862. https://doi.org/10.1021/ar6000445

[19] Xia X, Zhang YY, Chao D et al (2014) Solution synthesis of metal oxides for electrochemical energy storage applications. Nanoscale 6:5008–5048. https://doi.org/10.1039/C4NR00024B

[20] Zhang H, Ning H, Busbee J et al (2017) Electroplating lithium transition metal oxides. Sci Adv 3:e1602427. https://doi.org/10.1126/sciadv.1602427

[21] Elam JW, Dasgupta NP, Prinz FB (2011) ALD for clean energy conversion, utilization, and storage. MRS Bull 36:899–906. https://doi.org/10.1557/mrs.2011.265

[22] Dasgupta NP, Sun J, Liu C et al (2014) 25th Anniversary article: semiconductor nanowires—synthesis, characterization, and applications. Adv Mater 26:2137–2183. https://doi.org/10.1002/adma.201305929

[23] Zheng J, Zhao Q, Liu X et al (2019) Nonplanar electrode architectures for ultrahigh areal capacity batteries. ACS Energy Lett 4:271–275. https://doi.org/10.1021/acsenergylett.8b02131

[24] Rolison DR, Long JW, Lytle JC, Fischer AE, Rhodes CP, McEvoy TM, Bourg ME, Lubers AM (2009) Multifunctional 3D nanoarchitectures for energy storage and conversion. Chem Soc Rev 38:226–252. https://doi.org/10.1039/B801151F

[25] Sherrill SA, Banerjee P, Rubloff GW, Lee SB (2011) High to ultra-high power electrical energy storage. Phys Chem Chem Phys 13:20714–20723. https://doi.org/10.1039/c1cp22659b

[26] Lukatskaya MR, Dunn B, Gogotsi Y (2016) Multidimensional materials and device architectures for future hybrid energy storage. Nat Commun 7:1–13. https://doi.org/10.1038/ncomms12647

[27] Sun H, Zhu J, Baumann D, Peng L, Xu Y, Shakir I, Huang Y, Duan X (2019) Hierarchical 3D electrodes for electrochemical energy storage. Nat Rev Mater 4:45–60. https://doi.org/10.1038/s41578-018-0069-9

[28] Kang J, Zhang S, Zhang Z (2017) Three-dimensional binder-free nanoarchitectures for advanced pseudocapacitors. Adv Mater 29:1700515. https://doi.org/10.1002/adma.201700515

[29] Manthiram A (2003) Materials aspects: an overview. In: Nazri GA, Pistoia G (eds) Lithium batteries: science and technology. Springer, Berlin, pp 3–41

[30] Augustyn V, Simon P, Dunn B (2014) Pseudocapacitive oxide materials for high-rate electrochemical energy storage. Energy Environ Sci 7:1597. https://doi.org/10.1039/c3ee44164d

[31] Whittingham M (2000) Insertion electrodes as SMART materials: the first 25 years and future promises. Solid State Ionics 134:169–178. https://doi.org/10.1016/S0167-2738(00)00724-4

[32] Cabana J, Monconduit L, Larcher D, Palacín MR (2010) Beyond intercalation-based Li-ion batteries: the state of the art and challenges of electrode materials reacting through conversion reactions. Adv Mater 22:E170–E192. https://doi.org/10.1002/adma.201000717

[33] Whittingham MS (2004) Hydrogen motion in oxides: from insulators to bronzes. Solid State Ionics 168:255–263. https://doi.org/10.1016/j.ssi.2003.08.056

[34] Yang Y, Liu Q, Cao M, Ju Q, Wang H, Fu R, Ji H, Yang G (2019) Enhanced electrochemical performance of α-Fe_2O_3 grains grafted onto TiO_2–carbon nanofibers via a vapor–solid reaction as anode materials for Li-Ion batteries. Appl Surf Sci 463:322–330. https://doi.org/10.1016/j.apsusc.2018.08.171

[35] Huang Z-H, Song Y, Feng D-Y, Sun Z, Sun X, Liu X-X (2018) High mass loading MnO_2 with hierarchical nanostructures for supercapacitors. ACS Nano 12:3557–3567. https://doi.org/10.1021/acsnano.8b00621

[36] Wu C, Zhu Y, Ding M, Jia C, Zhang K (2018) Fabrication of plate-like MnO_2 with excellent cycle stability for supercapacitor electrodes. Electrochim Acta 291:249–255. https://doi.org/10.1016/j.electacta.2018.08.126

[37] Kim H-S, Cook JB, Lin H, Ko JS, Tolbert SH, Ozolins V, Dunn B (2017) Oxygen vacancies enhance pseudocapacitive charge storage properties of MoO_{3-x}. Nat Mater 16:454–460. https://doi.org/10.1038/nmat4810

[38] Augustyn V (2017) Tuning the interlayer of transition metal oxides for electrochemical energy storage. J Mater Res 32:2–15. https://doi.org/10.1557/jmr.2016.337

[39] Li X, Liu J, Banis MN, Lushington A, Li R, Cai M, Sun X (2014) Atomic layer deposition of solid-state electrolyte coated cathode materials with superior high-voltage cycling behavior for lithium ion battery application. Energy Environ Sci 7:768–778. https://doi.org/10.1039/c3ee42704h

[40] Wu Y, Wen Z, Li J (2011) Hierarchical carbon-coated $LiFePO_4$ nanoplate microspheres with high electrochemical performance for Li-ion batteries. Adv Mater 23:1126–1129. https://doi.org/10.1002/adma.201003713

[41] Liu T, Wang W, Yi M, Chen Q, Xu C, Cai D, Zhan H (2018) Metal-organic framework derived porous ternary $ZnCo_2O_4$ nanoplate arrays grown on carbon cloth as binder-free electrodes for lithium-ion batteries. Chem Eng J 354:454–462. https://doi.org/10.1016/j.cej.2018.08.037

[42] Xia X, Tu J, Zhang Y, Wang X, Gu C, Zhao X-B, Fan HJ (2012) High-quality metal oxide core/shell nanowire arrays on conductive substrates for electrochemical energy storage. ACS Nano 6:5531–5538. https://doi.org/10.1021/nn301454q

[43] Lim GJH, Liu X, Guan C, Wang J (2018) Co/Zn bimetallic oxides derived from metal organic frameworks for high performance electrochemical energy storage. Electrochim Acta 291:177–187. https://doi.org/10.1016/j.electacta.2018.08.105

[44] Wang J, Dong L, Xu C, Ren D, Ma X, Kang F (2018) Polymorphous supercapacitors constructed from flexible three-dimensional carbon network/polyaniline/MnO_2 composite textiles. ACS Appl Mater Interfaces 10:10851–10859. https://doi.org/10.1021/acsami.7b19195

[45] Wu H, Xu M, Wang Y, Zheng G (2013) Branched Co_3O_4/Fe_2O_3 nanowires as high capacity lithium-ion battery anodes. Nano Res 6:167–173. https://doi.org/10.1007/s12274-013-0292-z

[46] Fleischmann S, Zeiger M, Quade A, Kruth A, Presser V (2018) Atomic layer-deposited molybdenum oxide/carbon nanotube hybrid electrodes: the influence of crystal structure on lithium-ion capacitor performance. ACS Appl Mater Interfaces 10:18675–18684. https://doi.org/10.1021/acsami.8b03233

[47] Wang L, Gu X, Zhao L, Wang B, Jia C, Xu J, Zhao Y, Zhang J (2019) ZnO@TiO_2 heterostructure arrays/carbon cloth by charge redistribution enhances performance in flexible anode for Li ion batteries. Electrochim Acta 295:107–112. https://doi.org/10.1016/j.electacta.2018.10.146

[48] Luo Y, Luo J, Jiang J et al (2012) Seed-assisted synthesis of highly ordered TiO_2@α-Fe_2O_3 core/shell arrays on carbon textiles for lithium-ion battery applications. Energy Environ Sci 5:6559. https://doi.org/10.1039/c2ee03396h

[49] Xu C, Li Z, Yang C et al (2016) An ultralong, highly oriented nickel-nanowire-array electrode scaffold for high-performance compressible pseudocapacitors. Adv Mater 28:4105–4110. https://doi.org/10.1002/adma.201505644

[50] Li Y-Q, Li J-C, Lang X-Y, Wen Z, Zheng W-T, Jiang Q (2017) Lithium ion breathable electrodes with 3D hierarchical architecture for ultrastable and high-capacity lithium storage. Adv Funct Mater 27:1700447. https://doi.org/10.1002/adfm.201700447

[51] Aricò AS, Bruce P, Scrosati B, Tarascon J-M, van Schalkwijk W (2005) Nanostructured materials for advanced energy conversion and storage devices. Nat Mater 4:366–377. https://doi.org/10.1038/nmat1368

[52] Sun Y, Liu N, Cui Y (2016) Promises and challenges of nanomaterials for lithium-based rechargeable batteries. Nat Energy 1:16071. https://doi.org/10.1038/nenergy.2016.71

[53] Zhang F, Qi L (2016) Recent progress in self-supported metal oxide nanoarray electrodes for advanced lithium-ion batteries. Adv Sci 3:1600049. https://doi.org/10.1002/advs.201600049

[54] Wang Y, Takahashi K, Shang H, Cao G (2005) Synthesis and electrochemical properties of vanadium pentoxide

nanotube arrays. J Phys Chem B 109:3085–3088. https://doi.org/10.1021/jp044286w

[55] Choudhary N, Li C, Chung H-S, Moore J, Thomas J, Jung Y (2016) High-performance one-body core/shell nanowire supercapacitor enabled by conformal growth of capacitive 2D WS_2 layers. ACS Nano 10:10726–10735. https://doi.org/10.1021/acsnano.6b06111

[56] Zhong Y, Ma Y, Guo Q, Liu J, Wang Y, Yang M, Xia H (2017) Controllable synthesis of TiO_2@Fe_2O_3 core–shell nanotube arrays with double-wall coating as superb lithium-ion battery anodes. Sci Rep 7:40927. https://doi.org/10.1038/srep40927

[57] Tang Y, Hong L, Wu Q, Li J, Hou G, Cao H, Wu L, Zheng G (2016) TiO_2(B) nanowire arrays on Ti foil substrate as three-dimensional anode for lithium-ion batteries. Electrochim Acta 195:27–33. https://doi.org/10.1016/j.electacta.2016.01.235

[58] Pawlitzek F, Althues H, Schumm B, Kaskel S (2017) Nanostructured networks for energy storage: vertically aligned carbon nanotubes (VACNT) as current collectors for high-power $Li_4Ti_5O_{12}$(LTO)//$LiMn_2O_4$(LMO) lithium-ion batteries. Batteries 3:37. https://doi.org/10.3390/batteries3040037

[59] Jhao J-J, Lin C-H, Yeh T-K, Wu H-C, Tsai M-C, Hsieh C-K (2017) The coaxial nanostructure of ruthenium oxide thin films coated onto the vertically grown graphitic nanofibers for electrochemical supercapacitor. Surf Coat Technol 320:263–269. https://doi.org/10.1016/j.surfcoat.2017.01.006

[60] Zhang H, Yu X, Braun PV (2011) Three-dimensional bicontinuous ultrafast-charge and-discharge bulk battery electrodes. Nat Nanotechnol 6:277–281. https://doi.org/10.1038/nnano.2011.38

[61] Wang J, Zhou H, Nanda J, Braun PV (2015) Three-dimensionally mesostructured Fe_2O_3 electrodes with good rate performance and reduced voltage hysteresis. Chem Mater 27:2803–2811. https://doi.org/10.1021/cm504365s

[62] Liu J, Wang J, Kim J et al (2015) High full-electrode basis capacity template-free 3D nanocomposite secondary battery anodes. Small 11:6265–6271. https://doi.org/10.1002/smll.201502538

[63] Liu J, Zheng Q, Goodman MD et al (2016) Graphene sandwiched mesostructured Li-ion battery electrodes. Adv Mater 28:7696–7702. https://doi.org/10.1002/adma.201600829

[64] Hou C, Lang X-Y, Han G-F et al (2013) Integrated solid/nanoporous copper/oxide hybrid bulk electrodes for high-performance lithium-ion batteries. Sci Rep 3:2878. https://doi.org/10.1038/srep02878

[65] Xiao S, Bi F, Zhao L, Wang L, Gai G (2017) Design and synthesis of H-TiO_2/MnO_2 core–shell nanotube arrays with high capacitance and cycling stability for supercapacitors. J Mater Sci 52:7744–7753. https://doi.org/10.1007/s10853-017-1034-5

[66] Sathiya M, Prakash AS, Ramesha K, Tarascon J, Shukla AK (2011) V_2O_5-anchored carbon nanotubes for enhanced electrochemical energy storage. J Am Chem Soc 133:16291–16299. https://doi.org/10.1021/ja207285b

[67] Wu Z-S, Zhou G, Yin L-C, Ren W, Li F, Cheng H-M (2012) Graphene/metal oxide composite electrode materials for energy storage. Nano Energy 1:107–131. https://doi.org/10.1016/j.nanoen.2011.11.001

[68] Xu Y, Lin Z, Zhong X, Huang X, Weiss NO, Huang Y, Duan X (2014) Holey graphene frameworks for highly efficient capacitive energy storage. Nat Commun 5:4554. https://doi.org/10.1038/ncomms5554

[69] Xu Y, Chen C-Y, Zhao Z et al (2015) Solution processable holey graphene oxide and its derived macrostructures for high-performance supercapacitors. Nano Lett 15:4605–4610. https://doi.org/10.1021/acs.nanolett.5b01212

[70] Sun H, Mei L, Liang J et al (2017) Three-dimensional holey-graphene/niobia composite architectures for ultra-high-rate energy storage. Science 356:599–604. https://doi.org/10.1126/science.aam5852

[71] Chen X, Xiao T, Wang S, Li J, Xiang P, Jiang L, Tan X (2019) Superior Li-ion storage performance of graphene decorated NiO nanowalls on Ni as anode for lithium ion batteries. Mater Chem Phys 222:31–36. https://doi.org/10.1016/j.matchemphys.2018.09.061

[72] Chen Y, Wang Y, Wang Z et al (2018) Densification by compaction as an effective low-cost method to attain a high areal lithium storage capacity in a CNT@Co_3O_4 sponge. Adv Energy Mater 8:1702981. https://doi.org/10.1002/aenm.201702981

[73] Zhang Z, Zhang X, Feng Y et al (2018) Fabrication of porous $ZnCo_2O_4$ nanoribbon arrays on nickel foam for high-performance supercapacitors and lithium-ion batteries. Electrochim Acta 260:823–829. https://doi.org/10.1016/j.electacta.2017.12.047

[74] Jadhav HS, Pawar SM, Jadhav AH, Thorat GM, Seo JG (2016) Hierarchical mesoporous 3D flower-like $CuCo_2O_4$/NF for high-performance electrochemical energy storage. Sci Rep 6:31120. https://doi.org/10.1038/srep31120

[75] Zhou D, Cheng P, Luo J, Xu W, Li J, Yuan D (2017) Facile synthesis of graphene@$NiMoO_4$ nanosheet arrays on Ni foam for a high-performance asymmetric supercapacitor. J Mater Sci 52:13909–13919. https://doi.org/10.1007/s10853-017-1467-x

[76] Xia X, Chao D, Ng CF, Lin J, Fan Z, Zhang H, Shen ZX, Fan HJ (2015) VO_2 nanoflake arrays for supercapacitor and Li-ion battery electrodes: performance enhancement by hydrogen molybdenum bronze as an efficient shell material. Mater Horizons 2:237–244. https://doi.org/10.1039/C4MH00212A

[77] Lang X, Zhang H, Xue X et al (2018) Rational design of $La_{0.85}Sr_{0.15}MnO_3$@$NiCo_2O_4$ core–shell architecture supported on Ni foam for high performance supercapacitors. J Power Sources 402:213–220. https://doi.org/10.1016/j.jpowsour.2018.09.040

[78] Yuan J, Chen C, Hao Y et al (2017) Three-dimensionally porous $CoMn_2O_4$ thin films grown on Ni foams for high-performance lithium-ion battery anodes. J Mater Sci 52:5751–5758. https://doi.org/10.1007/s10853-017-0810-6

[79] Li L, Zhang YQ, Liu XY et al (2014) One-dimension $MnCo_2O_4$ nanowire arrays for electrochemical energy storage. Electrochim Acta 116:467–474. https://doi.org/10.1016/j.electacta.2013.11.081

[80] Wang J, Zhang H, Lv X, Nie K, Gao X, Zhong J, Sun X (2016) Self-supported ultrathin mesoporous $CoFe_2O_4$/CoO nanosheet arrays assembled from nanowires with enhanced lithium storage performance. J Mater Sci 51:6590–6599. https://doi.org/10.1007/s10853-016-9902-y

[81] Zhang F, Yang C, Guan H, Hu Y, Jin C, Zhou H, Qi L (2018) 3D copper foam@FeO_x nanoarrays as a high areal capacity and stable electrode for lithium-ion batteries. ACS Appl Energy Mater. https://doi.org/10.1021/acsaem.8b01024

[82] Um JH, Choi M, Park H, Cho Y-H, Dunand DC, Choe H, Sung Y-E (2016) 3D macroporous electrode and high-performance in lithium-ion batteries using SnO_2 coated on Cu foam. Sci Rep 6:18626. https://doi.org/10.1038/srep18626

[83] Wang J, Wang G, Wang H (2015) Flexible free-standing Fe_2O_3/graphene/carbon nanotubes hybrid films as anode materials for high performance lithium-ion batteries. Electrochim Acta 182:192–201. https://doi.org/10.1016/j.electacta.2015.09.080

[84] Xu Y, Xuan H, Gao J et al (2018) Hierarchical three-dimensional $NiMoO_4$-anchored rGO/Ni foam as advanced electrode material with improved supercapacitor performance. J Mater Sci 53:8483–8498. https://doi.org/10.1007/s10853-018-2171-1

[85] Zhang H, Deng X, Huang H et al (2018) Hetero-structure arrays of $NiCoO_2$ nanoflakes@nanowires on 3D graphene/nickel foam for high-performance supercapacitors. Electrochim Acta 289:193–203. https://doi.org/10.1016/j.electacta.2018.08.071

[86] Zhai X, Mao Z, Zhao G, Rooney D, Zhang N, Sun K (2018) Nanoflake δ-MnO_2 deposited on carbon nanotubes-graphene-Ni foam scaffolds as self-standing three-dimensional porous anodes for high-rate-performance lithium-ion batteries. J Power Sources 402:373–380. https://doi.org/10.1016/j.jpowsour.2018.09.057

[87] Jia H, Cai Y, Zheng X et al (2018) Mesostructured carbon nanotube-on-MnO_2 nanosheet composite for high-performance supercapacitors. ACS Appl Mater Interfaces 10:38963–38969. https://doi.org/10.1021/acsami.8b14109

[88] Xia X, Chao D, Zhang Y et al (2016) Generic synthesis of carbon nanotube branches on metal oxide arrays exhibiting stable high-rate and long-cycle sodium-ion storage. Small 12:3048–3058. https://doi.org/10.1002/smll.201600633

[89] Chao D, Xia X, Liu J et al (2014) A V_2O_5/conductive-polymer core/shell nanobelt array on three-dimensional graphite foam: a high-rate, ultrastable, and freestanding cathode for lithium-ion batteries. Adv Mater 26:5794–5800. https://doi.org/10.1002/adma.201400719

[90] Lin L, Tang S, Zhao S, Peng X, Hu N (2017) Hierarchical three-dimensional $FeCo_2O_4$@MnO_2 core–shell nanosheet arrays on nickel foam for high-performance supercapacitor. Electrochim Acta 228:175–182. https://doi.org/10.1016/j.electacta.2017.01.022

[91] Luo J, Xia X, Luo Y et al (2013) Rationally designed hierarchical TiO_2@Fe_2O_3 hollow nanostructures for improved lithium ion storage. Adv Energy Mater 3:737–743. https://doi.org/10.1002/aenm.201200953

[92] Wang B, Li S, Wu X, Liu J, Tian W (2016) Hierarchical $NiMoO_4$ nanowire arrays supported on macroporous graphene foam as binder-free 3D anodes for high-performance lithium storage. Phys Chem Chem Phys 18:908–915. https://doi.org/10.1039/C5CP04820F

[93] Chen X, Zhu H, Chen Y-C, Shang Y, Cao A, Hu L, Rubloff GW (2012) MWCNT/V_2O_5 core/shell sponge for high areal capacity and power density li-ion cathodes. ACS Nano 6:7948–7955. https://doi.org/10.1021/nn302417x

[94] Ko JS, Sassin MB, Parker JF, Rolison DR, Long JW (2018) Combining battery-like and pseudocapacitive charge storage in 3D MnO_x@carbon electrode architectures for zinc-ion cells. Sustain Energy Fuels 2:626–636. https://doi.org/10.1039/C7SE00540G

[95] Guan C, Liu J, Wang Y, Mao L, Fan Z, Shen Z, Zhang H, Wang J (2015) Iron oxide-decorated carbon for supercapacitor anodes with ultrahigh energy density and outstanding cycling stability. ACS Nano 9:5198–5207. https://doi.org/10.1021/acsnano.5b00582

[96] Liu B, Zhang J, Wang X, Chen G, Chen D, Zhou C, Shen G (2012) Hierarchical three-dimensional $ZnCo_2O_4$ nanowire arrays/carbon cloth anodes for a novel class of high-performance flexible lithium-ion batteries. Nano Lett 12:3005–3011. https://doi.org/10.1021/nl300794f

[97] Huang Z-H, Song Y, Liu X-X (2019) Boosting operating voltage of vanadium oxide-based symmetric aqueous supercapacitor to 2 V. Chem Eng J 358:1529–1538. https://doi.org/10.1016/j.cej.2018.10.136

[98] Ma L, Fan H, Wei X et al (2018) Towards high areal capacitance, rate capability, and tailorable supercapacitors: Co_3O_4@polypyrrole core–shell nanorod bundle array electrodes. J Mater Chem A 6:19058–19065. https://doi.org/10.1039/C8TA07477A

[99] Qu G, Cheng J, Li X, Yuan D, Chen P, Chen X, Wang B, Peng H (2016) A fiber supercapacitor with high energy density based on hollow graphene/conducting polymer fiber electrode. Adv Mater 28:3646–3652. https://doi.org/10.1002/adma.201600689

[100] Noh J, Yoon C-M, Kim YK, Jang J (2017) High performance asymmetric supercapacitor twisted from carbon fiber/MnO_2 and carbon fiber/MoO_3. Carbon 116:470–478. https://doi.org/10.1016/j.carbon.2017.02.033

[101] Shah HU, Wang F, Javed MS, Ahmad MA, Saleem M, Zhan J, Khan ZUH, Li Y (2018) In-situ growth of MnO_2 nanorods forest on carbon textile as efficient electrode material for supercapacitors. J Energy Storage 17:318–326. https://doi.org/10.1016/j.est.2018.03.015

[102] Zhu Y, Huang Y, Wang M, Wang K, Yu M, Chen X, Zhang Z (2018) Novel carbon coated core–shell heterostructure $NiCo_2O_4$@NiO grown on carbon cloth as flexible lithium-ion battery anodes. Ceram Int 44:21690–21698. https://doi.org/10.1016/j.ceramint.2018.08.257

[103] Zhang L, Zhang Y, Huang S et al (2018) Co_3O_4/Ni-based MOFs on carbon cloth for flexible alkaline battery-supercapacitor hybrid devices and near-infrared photocatalytic hydrogen evolution. Electrochim Acta 281:189–197. https://doi.org/10.1016/j.electacta.2018.05.162

[104] Shen L, Che Q, Li H, Zhang X (2014) Mesoporous $NiCo_2O_4$ nanowire arrays grown on carbon textiles as binder-free flexible electrodes for energy storage. Adv Funct Mater 24:2630–2637. https://doi.org/10.1002/adfm.201303138

[105] Zhu C, Usiskin RE, Yu Y, Maier J (2017) The nanoscale circuitry of battery electrodes. Science 358:eaao2808. https://doi.org/10.1126/science.aao2808

[106] Wang R, Xu C, Sun J, Gao L, Lin C (2013) Flexible free-standing hollow Fe_3O_4/graphene hybrid films for lithium-ion batteries. J Mater Chem A 1:1794–1800. https://doi.org/10.1039/C2TA00753C

[107] Zhou G, Wang D-W, Hou P-X, Li W, Li N, Liu C, Li F, Cheng H-M (2012) A nanosized Fe_2O_3 decorated single-walled carbon nanotube membrane as a high-performance flexible anode for lithium ion batteries. J Mater Chem 22:17942. https://doi.org/10.1039/c2jm32893c

[108] Haichao L, Haoyi L, Bubakir MM, Weimin Y, Barhoum A (2018) Engineering nanofibers as electrode and membrane materials for batteries, supercapacitors, and fuel cells. In: Barhoum A, Bechelany M, Makhlouf A (eds) Handbook of nanofibers. Springer, Cham, pp 1–27

[109] Liu X, Jiang Y, Li K, Xu F, Zhang P, Ding Y (2019) Electrospun free-standing N-doped C@SnO_2 anode paper for flexible Li-ion batteries. Mater Res Bull 109:41–48. https://doi.org/10.1016/j.materresbull.2018.09.023

[110] Cuan J, Zhang F, Zhang H et al (2018) Heterostructure manipulation toward ameliorating electrodes for better lithium storage capability. ACS Sustain Chem Eng 6:17267–17276. https://doi.org/10.1021/acssuschemeng.8b04685

[111] Kong D, Li X, Zhang Y et al (2016) Encapsulating V_2O_5 into carbon nanotubes enables the synthesis of flexible high-performance lithium ion batteries. Energy Environ Sci 9:906–911. https://doi.org/10.1039/C5EE03345D

[112] Rolison DR, Dunn B (2001) Electrically conductive oxide aerogels: new materials in electrochemistry. J Mater Chem 11:963–980. https://doi.org/10.1039/b007591o

[113] Hong J-Y, Bak BM, Wie JJ, Kong J, Park HS (2015) Reversibly compressible, highly elastic, and durable graphene aerogels for energy storage devices under limiting conditions. Adv Funct Mater 25:1053–1062. https://doi.org/10.1002/adfm.201403273

[114] Chen D, Peng L, Yuan Y et al (2017) Two-dimensional holey Co_3O_4 nanosheets for high-rate alkali-ion batteries: from rational synthesis to in situ probing. Nano Lett 17:3907–3913. https://doi.org/10.1021/acs.nanolett.7b01485

[115] Liu L, Yang X, Lv C, Zhu A, Zhu X, Guo S, Chen C, Yang D (2016) Seaweed-derived route to Fe_2O_3 hollow nanoparticles/N-doped graphene aerogels with high lithium ion storage performance. ACS Appl Mater Interfaces 8:7047–7053. https://doi.org/10.1021/acsami.5b12427

[116] Huang H, Wang X, Tervoort E, Zeng G, Liu T, Chen X, Sologubenko A, Niederberger M (2018) Nano-sized structurally disordered metal oxide composite aerogels as high-power anodes in hybrid supercapacitors. ACS Nano 12:2753–2763. https://doi.org/10.1021/acsnano.7b09062

[117] Sun W, Gao G, Zhang K, Liu Y, Wu G (2018) Self-assembled 3D N-CNFs/V_2O_5 aerogels with core/shell nanostructures through vacancies control and seeds growth as an outstanding supercapacitor electrode material. Carbon 132:667–677. https://doi.org/10.1016/j.carbon.2018.03.004

[118] Wang R, Xu C, Sun J, Gao L, Yao H (2014) Solvothermal-induced 3D macroscopic SnO_2/nitrogen-doped graphene aerogels for high capacity and long-life lithium storage.

ACS Appl Mater Interfaces 6:3427–3436. https://doi.org/10.1021/am405557c

[119] Zhou Y, Wen L, Zhan K, Yan Y, Zhao B (2018) Three-dimensional porous graphene/nickel cobalt mixed oxide composites for high-performance hybrid supercapacitor. Ceram Int 44:21848–21854. https://doi.org/10.1016/j.ceramint.2018.08.292

[120] Liu M, Liu Y, Zhang Y, Li Y, Zhang P, Yan Y, Liu T (2016) Octahedral tin dioxide nanocrystals anchored on vertically aligned carbon aerogels as high capacity anode materials for lithium-ion batteries. Sci Rep 6:31496. https://doi.org/10.1038/srep31496

[121] Gao X-T, Liu Y-T, Zhu X-D, Yan D-J, Wang C, Feng Y-J, Sun K-N (2018) V_2O_5 nanoparticles confined in three-dimensionally organized, porous nitrogen-doped graphene frameworks: flexible and free-standing cathodes for high performance lithium storage. Carbon 140:218–226. https://doi.org/10.1016/j.carbon.2018.08.060

[122] Yao B, Chandrasekaran S, Zhang J et al (2019) Efficient 3D printed pseudocapacitive electrodes with ultrahigh MnO_2 loading. Joule 3:459–470. https://doi.org/10.1016/j.joule.2018.09.020

[123] Takada K (2013) Progress and prospective of solid-state lithium batteries. Acta Mater 61:759–770. https://doi.org/10.1016/j.actamat.2012.10.034

[124] Manthiram A, Yu X, Wang S (2017) Lithium battery chemistries enabled by solid-state electrolytes. Nat Rev Mater 2:16103. https://doi.org/10.1038/natrevmats.2016.103

[125] Zhang B, Tan R, Yang L, Zheng J, Zhang K, Mo S, Lin Z, Pan F (2018) Mechanisms and properties of ion-transport in inorganic solid electrolytes. Energy Storage Mater 10:139–159. https://doi.org/10.1016/j.ensm.2017.08.015

[126] Xiao Y, Miara LJ, Wang Y, Ceder G (2019) Computational screening of cathode coatings for solid-state batteries. Joule 2:1–24. https://doi.org/10.1016/j.joule.2019.02.006

[127] Han X, Gong Y, Fu K et al (2016) Negating interfacial impedance in garnet-based solid-state Li metal batteries. Nat Mater 16:572–579. https://doi.org/10.1038/nmat4821

[128] Sharafi A, Meyer HM, Nanda J, Wolfenstine J, Sakamoto J (2016) Characterizing the Li–$Li_7La_3Zr_2O_{12}$ interface stability and kinetics as a function of temperature and current density. J Power Sources 302:135–139. https://doi.org/10.1016/j.jpowsour.2015.10.053

[129] Cheng EJ, Sharafi A, Sakamoto J (2017) Intergranular Li metal propagation through polycrystalline $Li_{6.25}Al_{0.25}La_3Zr_2O_{12}$ ceramic electrolyte. Electrochim Acta 223:85–91. https://doi.org/10.1016/j.electacta.2016.12.018

[130] Yu S, Schmidt RD, Garcia-Mendez R, Herbert E, Dudney NJ, Wolfenstine JB, Sakamoto J, Siegel DJ (2016) Elastic properties of the solid electrolyte $Li_7La_3Zr_2O_{12}$ (LLZO). Chem Mater 28:197–206. https://doi.org/10.1021/acs.chemmater.5b03854

[131] Wang C, Li X, Zhao Y et al (2019) Manipulating interfacial nanostructure to achieve high-performance all-solid-state lithium-ion batteries. Small Methods 1900261:1900261. https://doi.org/10.1002/smtd.201900261

[132] Bachman JC, Muy S, Grimaud A et al (2016) Inorganic solid-state electrolytes for lithium batteries: mechanisms and properties governing ion conduction. Chem Rev 116:140–162. https://doi.org/10.1021/acs.chemrev.5b00563

[133] Meier K, Laino T, Curioni A (2014) Solid-state electrolytes: Revealing the mechanisms of Li-ion conduction in tetragonal and cubic LLZO by first-principles calculations. J Phys Chem C 118:6668–6679. https://doi.org/10.1021/jp5002463

[134] Augustyn V, McDowell MT, Vojvodic A (2018) Toward an atomistic understanding of solid-state electrochemical interfaces for energy storage. Joule 2:2189–2193. https://doi.org/10.1016/j.joule.2018.10.014

[135] Janek J, Zeier WG (2016) A solid future for battery development. Nat Energy 1:16141. https://doi.org/10.1038/nenergy.2016.141

[136] Hao F, Han F, Liang Y, Wang C, Yao Y (2018) Architectural design and fabrication approaches for solid-state batteries. MRS Bull 43:775–781. https://doi.org/10.1557/mrs.2018.211

[137] Kato Y, Hori S, Saito T et al (2016) High-power all-solid-state batteries using sulfide superionic conductors. Nat Energy 1:16030. https://doi.org/10.1038/nenergy.2016.30

[138] van den Broek J, Afyon S, Rupp JLM (2016) Interface-engineered all-solid-state Li-ion batteries based on garnet-type fast Li^+ conductors. Adv Energy Mater 6:1600736. https://doi.org/10.1002/aenm.201600736

[139] Han F, Yue J, Chen C et al (2018) Interphase engineering enabled all-ceramic lithium battery. Joule 2:497–508. https://doi.org/10.1016/j.joule.2018.02.007

[140] Sakuda A, Takeuchi T, Kobayashi H (2016) Electrode morphology in all-solid-state lithium secondary batteries consisting of $LiNi_{1/3}Co_{1/3}Mn_{1/3}O_2$ and Li_2S-P_2S_5 solid electrolytes. Solid State Ionics 285:112–117. https://doi.org/10.1016/j.ssi.2015.09.010

[141] Sakuda A, Hayashi A, Tatsumisago M (2017) Recent progress on interface formation in all-solid-state batteries. Curr Opin Electrochem 6:108–114. https://doi.org/10.1016/j.coelec.2017.10.008

[142] Sakuda A, Hayashi A, Tatsumisago M (2013) Sulfide solid electrolyte with favorable mechanical property for all-solid-state lithium battery. Sci Rep 3:2261. https://doi.org/10.1038/srep02261

[143] Machida N, Kashiwagi J, Naito M, Shigematsu T (2012) Electrochemical properties of all-solid-state batteries with ZrO_2-coated $LiNi_{1/3}Mn_{1/3}Co_{1/3}O_2$ as cathode materials. Solid State Ionics 225:354–358. https://doi.org/10.1016/j.ssi.2011.11.026

[144] Okada K, Machida N, Naito M, Shigematsu T, Ito S, Fujiki S, Nakano M, Aihara Y (2014) Preparation and electrochemical properties of $LiAlO_2$-coated $Li(Ni_{1/3}Mn_{1/3}Co_{1/3})O_2$ for all-solid-state batteries. Solid State Ionics 255:120–127. https://doi.org/10.1016/j.ssi.2013.12.019

[145] Kitaura H, Hayashi A, Tadanaga K, Tatsumisago M (2010) Electrochemical performance of all-solid-state lithium secondary batteries with Li–Ni–Co–Mn oxide positive electrodes. Electrochim Acta 55:8821–8828. https://doi.org/10.1016/j.electacta.2010.07.066

[146] Ohta N, Takada K, Sakaguchi I, Zhang L, Ma R, Fukuda K, Osada M, Sasaki T (2007) $LiNbO_3$-coated $LiCoO_2$ as cathode material for all solid-state lithium secondary batteries. Electrochem Commun 9:1486–1490. https://doi.org/10.1016/j.elecom.2007.02.008

[147] Sun S, Xia Q, Liu J et al (2019) Self-standing oxygen-deficient α-MoO_{3-x} nanoflake arrays as 3D cathode for advanced all-solid-state thin film lithium batteries. J Mater 5:229–236. https://doi.org/10.1016/j.jmat.2019.01.001

[148] Xu S, McOwen DW, Zhang L et al (2018) All-in-one lithium-sulfur battery enabled by a porous-dense-porous garnet architecture. Energy Storage Mater 15:458–464. https://doi.org/10.1016/j.ensm.2018.08.009

[149] Gong Y, Fu K, Xu S et al (2018) Lithium-ion conductive ceramic textile: a new architecture for flexible solid-state lithium metal batteries. Mater Today 21:594–601. https://doi.org/10.1016/j.mattod.2018.01.001

[150] Minke C, Kunz U, Turek T (2017) Carbon felt and carbon fiber—a techno-economic assessment of felt electrodes for redox flow battery applications. J Power Sources 342:116–124. https://doi.org/10.1016/j.jpowsour.2016.12.039

[151] Hakimian A, Kamarthi S, Erbis S, Abraham KM, Cullinane TP, Isaacs JA (2015) Economic analysis of CNT lithium-ion battery manufacturing. Environ Sci Nano 2:463–476. https://doi.org/10.1039/c5en00078e

Publisher's Note Springer Nature remains neutral with regard to jurisdictional claims in published maps and institutional affiliations.